

# Contents

<b>Introduction</b>	<b>1</b>
<b>1 Standard Model and Supersymmetry</b>	<b>2</b>
1.1 The Standard Model . . . . .	2
1.1.1 Quantum Field Theories . . . . .	2
1.1.2 Fundamental interactions . . . . .	3
1.1.3 The Higgs mechanism . . . . .	6
1.2 The limitations of the Standard Model . . . . .	9
1.2.1 The Higgs hierarchy problem . . . . .	9
1.2.2 Dark matter . . . . .	11
1.2.3 More open issues . . . . .	12
1.3 Supersymmetry . . . . .	13
1.3.1 Supersymmetric theories . . . . .	13
1.3.2 The Minimal Supersymmetric Standard Model (MSSM) . . . . .	15
1.3.3 SUSY as a solution to the hierarchy problem . . . . .	20
1.3.4 SUSY models with spontaneous $R$ -parity breaking . . . . .	22
1.4 SUSY searches at the LHC . . . . .	24
1.4.1 Experimental challenges and benchmark models . . . . .	24
1.4.2 Phenomenology of third generation squarks . . . . .	27
<b>2 LHC and ATLAS</b>	<b>31</b>
2.1 The LHC accelerator . . . . .	31
2.1.1 Particle accelerators . . . . .	31
2.1.2 Physics at hadron colliders . . . . .	32
2.1.3 The purpose of the LHC . . . . .	34
2.1.4 The CERN accelerator complex and the LHC . . . . .	36
2.2 The LHC experiments . . . . .	37
2.2.1 General-purpose experiments . . . . .	39

2.3	The ATLAS detector	40
2.3.1	Coordinate system and event display	41
2.3.2	Magnet system	42
2.3.3	Inner Detector	43
2.3.4	Calorimeter system	46
2.3.5	Muon Spectrometer	49
2.4	Trigger and data processing	51
2.4.1	Trigger system	51
2.4.2	Data acquisition and control system	53
2.5	ATLAS physics program	53
2.5.1	Standard Model and Higgs measurements	53
2.5.2	Supersymmetry searches	54
2.5.3	Other searches	54
<b>3</b>	<b>Object reconstruction</b>	<b>55</b>
<b>4</b>	<b>B-tagging calibration with Monte Carlo simulations</b>	<b>56</b>
<b>5</b>	<b>Search for bottom squark pair-production</b>	<b>57</b>
<b>6</b>	<b>Search for top squark pair-production in RPV U1(B-L) scenarios</b>	<b>58</b>
<b>7</b>	<b>Conclusions</b>	<b>59</b>
<b>A</b>	<b>Statistical tools</b>	<b>60</b>

# **Introduction**

blablabla.....

# Chapter 1

## Standard Model and Supersymmetry

This chapter provides a theoretical introduction to the physics topics discussed in the thesis. Section 1.1 presents the main features of the Standard Model of the elementary particles, while Section 1.2 is dedicated to a discussion of the open problems in particle physics that are calling for an extension of the theory. Supersymmetry is introduced in Section 1.3, which includes a discussion of the main motivations for light third generation squarks at the TeV scale. Finally, Section 1.4 presents the typical experimental signatures of third generation squarks in high energy physics experiments.

### 1.1 The Standard Model

The Standard Model of the elementary particles is the theory that describes the phenomenology of fundamental fields and interactions. It includes all the particles that have been directly observed in high energy physics experiments, classifying them based on their mass, spin and interaction properties.

#### 1.1.1 Quantum Field Theories

The Standard Model is a paradigm of a Quantum Field Theory (QFT), a major theoretical construction of the 20<sup>th</sup> century that unifies the principles of special relativity and quantum mechanics. Elementary particles are described as excitations of quantum fields embedded in a four-dimensional Minkowski spacetime, so they can be classified based on their behaviour under Poincaré transformations: fermions are particles with half-integer spin,  $\frac{1}{2}$  in units of  $\hbar$ , while bosons have integer spin, 0 for scalars and 1 for vectors. Another relevant property of the fields is their mass, that determines the propagation of the particles in the spacetime in absence of interactions.

The theory makes use of the Lagrangian formalism, where all the necessary information to derive the field dynamics is included in a Lagrangian density function  $\mathcal{L}$ :

$$\mathcal{L}_{tot} = \mathcal{L}_{free} + \mathcal{L}_{int} \quad (1.1)$$

In the above equation the full expression of  $\mathcal{L}$  is split into a kinetic term and an interaction term, which describe the spacetime evolution of the free fields and the way in which they are coupled.

### 1.1.2 Fundamental interactions

Once the spacetime properties of the fields are defined, the following step is to examine their interactions. At the present state of knowledge, any interaction observed in nature can be reduced to four fundamental forces: weak and strong interactions, electromagnetism and gravity. Among these only the latter is not included in the Standard Model, but its measured strength is extremely low compared to the others, so its impact is negligible in any realistic particle physics experiment.

As discussed in detail in Ref. [1], all the interaction terms of the Standard Model can be derived by imposing that the Lagrangian is invariant under special local transformations of the fields known as gauge transformations. When the field content of the theory is established, the choice of a particular gauge symmetry fixes the structure of the couplings between the fermions and new spin-1 vector fields, commonly referred to as gauge fields or mediators of the force. The new fields are introduced in order to preserve the invariance of the Lagrangian under the gauge transformation, so there is a direct correspondence between the imposed symmetry and the properties of the interaction. The full gauge symmetry group of the Standard Model is

$$SU(3)_C \otimes SU(2)_L \otimes U(1)_Y \quad (1.2)$$

where  $SU(3)_C$  is the color symmetry of the strong interaction and  $SU(2)_L \otimes U(1)_Y$  is the electroweak symmetry.

Having identified four fundamental forces allows to add an extra classification of the elementary fields. Fermions are referred to as leptons if they only interact via electromagnetic and weak (electroweak) force, while they are called quarks if they also experience the strong interaction. A crucial difference between the two types of objects, that emerges as a consequence of the different properties of electroweak and strong force, is that only elementary leptons can be observed as free particles, while quarks are always observed in bound states called hadrons. Hadrons are known as mesons if they are

bosons, such as pions or kaons, while they are called baryons if they are fermions, with the most common examples being protons or neutrons. Figure 1.1 shows the presently known elementary particles of the Standard Model, classifying them in quarks, leptons, gauge bosons and an additional scalar boson, the Higgs.

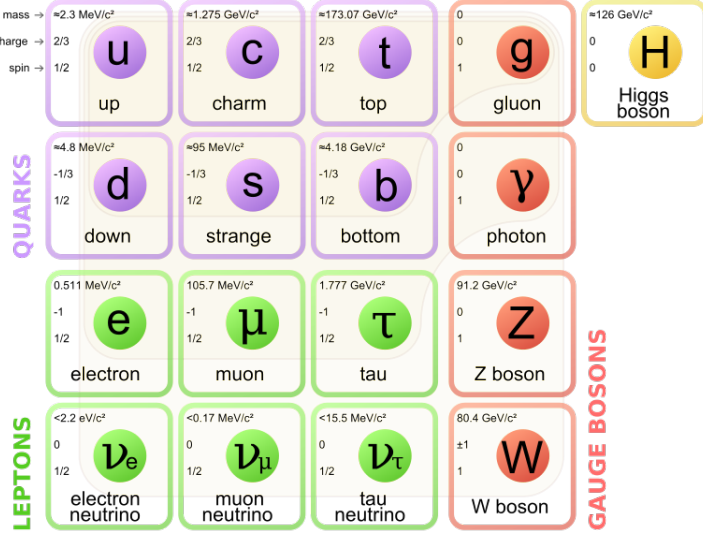


Figure 1.1: Elementary particles in the Standard Model.

## Electroweak force

The first fundamental interaction described by the Standard Model is the electroweak force, which appears in the theory as a unified description of electromagnetic and weak forces. The electroweak force is based on the  $SU(2)_L \otimes U(1)_Y$  symmetry group [2–4] introduced by Glashow, Weinberg and Salam to combine the features of Quantum Electrodynamics (QED) and of a formal description of the Fermi theory of weak interactions where the  $SU(2)_L$  structure had first emerged. The  $L$  of the  $SU(2)_L$  group stands for *left*: only the left chiral components of the fermion fields (spinors) carry a weak isospin charge and therefore experience the weak interaction.

When the  $SU(2)_L \otimes U(1)_Y$  symmetry is imposed in the Lagrangian four vector bosons are obtained: three  $W_i^\mu$  bosons originating from the  $SU(2)_L$  part and one  $B^\mu$  boson originating from  $U(1)_Y$ . Mass eigenstates are then derived by mixing the four gauge bosons as follows:

$$\begin{aligned}
 W_\pm^\mu &= \frac{W_1^\mu \mp iW_2^\mu}{\sqrt{2}} \\
 A^\mu &= B^\mu \cos \theta_W + W_3^\mu \sin \theta_W \\
 Z^\mu &= W_3^\mu \cos \theta_W - B^\mu \sin \theta_W
 \end{aligned} \tag{1.3}$$

In the equations above the mediators of electromagnetic and weak interactions, the photon  $A$ , the  $Z$  and the two  $W^\pm$  bosons, appear as linear combinations of the eigenstates of  $SU(2)_L$  and  $U(1)_Y$ . The last two rows contain a fundamental parameter of the Standard Model, the Weinberg angle  $\theta_W$ , whose value has been accurately measured by various high energy physics experiments at different energy scales. In addition, to obtain the correct quantum numbers of each Standard Model particle, the hypercharge  $Y$  introduced in the  $SU(2)_L \otimes U(1)_Y$  group needs to be related to the electric charge  $Q$  and the weak isospin  $T_3$  through the Gell Mann-Nishijima equation:

$$Q = \frac{Y}{2} + T_3 \quad (1.4)$$

As extensively tested in the experiments,  $W^\pm$  bosons carry an electric charge of  $Q = \pm 1$  and are only coupled to left handed fermions through their weak isospin charge  $T_3$ .  $Z$  bosons are instead electrically neutral and couple differently to left and right handed fermions: for left handed fermions the coupling depends on both  $T_3$  and  $Q$ , while for right handed fermions it is only proportional to  $Q$ .

### Strong force

Together with the electroweak force, the Standard Model provides a full description of strong interactions. The corresponding field theory, Quantum Chromodynamics (QCD), is based on the  $SU(3)_C$  symmetry group, which introduces eight vector boson mediators known as gluons [5]. The charge associated with the  $SU(3)$  symmetry is the colour, C, and the elementary fermions that carry it are the quarks in Figure 1.1. Unlike photons in QED, gluons carry colour charge as a result of the non-abelian character of  $SU(3)_C$ . This implies that they are allowed to couple with each other, with significant impact on the phenomenological properties of the interaction.

The QCD Lagrangian and the masses of the quarks can be used to compute the scale evolution of the coupling constant  $\alpha_s$ , that can be expressed as a function of the transferred energy  $\mu$ :

$$\alpha_s(\mu^2) = \frac{12\pi}{(33 - 2n_f) \log\left(\frac{\mu^2}{\Lambda_{QCD}^2}\right)} \quad (1.5)$$

where  $n_f$  is the number of quarks with mass below  $\mu$  and  $\Lambda_{QCD} \sim 200$  MeV is a characteristic scale of the theory. When the quark content of the Standard Model is considered, equation 1.5 shows that the coupling constant  $\alpha_s$  decreases as a function of the characteristic scale of the interactions. On the other hand, the coupling diverges rapidly when  $\mu$  decreases and approaches  $\Lambda$ . This implies that the theory is only perturbative at high

energy scales, because the necessary condition  $\alpha_s \ll 1$  is only true for  $\mu \gg \Lambda_{QCD}$ . In addition, three more essential features of QCD emerge:

- *Asymptotic freedom*:  $\alpha_s \rightarrow 0$  as  $\mu \rightarrow \infty$ , so in the high energy limit the strength of the interaction becomes negligible and quarks behave as free particles [6].
- *Confinement*: at low energies (or large distances) the coupling strength increases rapidly, keeping the quarks strongly bound to each other and implying that only colour singlet states can be observed as free particles.
- *Hadronisation*: when two coloured objects are split, the extraction of a new pair of hadrons from the vacuum soon becomes energetically preferable with respect to a further increase in distance.

Hadronisation is responsible for the production of jets at high energy physics experiments, where quarks of gluons with high momentum form cascades of hadronic particles that terminate only when no more energy is left to extract more objects from the vacuum.

### 1.1.3 The Higgs mechanism

The theory of electroweak and strong interactions describes the experimental data with remarkable precision. However, a major limitation comes from the fact that its fundamental premises, gauge invariance and chiral symmetry, are not compatible with the presence of mass terms in the Lagrangian. If no extra feature is added, a Lagrangian with the interactions described in Section 1.1.2 predicts all the Standard Model particles to be massless, in clear contrast with the experimental evidence.

The problem of introducing the masses of the particles without spoiling gauge and chiral symmetries can be solved by a spontaneous symmetry breaking mechanism [7–9]. The idea is to postulate the existence of an electrically neutral scalar complex field, the Higgs field, whose interaction with the other particles is responsible for their masses. The Lagrangian is expanded with an additional term

$$\mathcal{L}_\phi = (D^\mu \phi)^\dagger (D_\mu \phi) - V(\phi^\dagger \phi) \quad (1.6)$$

where  $\phi$  is the Higgs field, a weak isospin doublet with hypercharge  $Y = 1$ , and  $D_\mu$  is the covariant derivative that contains the electroweak gauge fields  $W_i^\mu$  and  $B^\mu$ . The first component of  $\phi$  has electric charge +1 while the second is neutral, and the full expression is given by

$$\phi = \begin{pmatrix} \phi^\dagger \\ \phi^0 \end{pmatrix} = \frac{1}{\sqrt{2}} \begin{pmatrix} \phi_1 + i\phi_2 \\ \phi_3 + i\phi_4 \end{pmatrix} \quad (1.7)$$

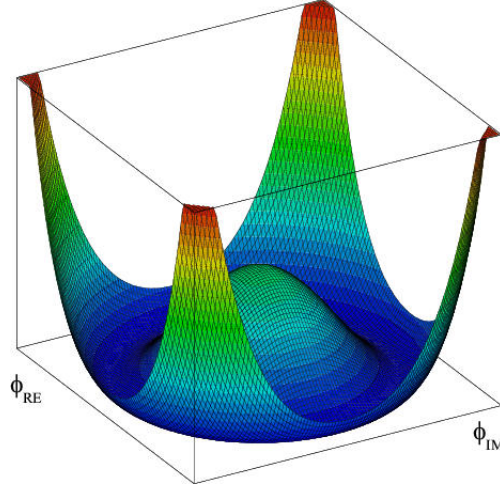


Figure 1.2: Shape of the Higgs potential for a one-dimensional complex field  $\phi$  with  $\lambda > 0$  and  $\mu^2 < 0$ .

The term  $V$  in the Lagrangian 1.6 is the Higgs potential and has the form

$$V(\phi^\dagger \phi) = \mu^2 \phi^\dagger \phi + \lambda (\phi^\dagger \phi)^2 \quad (1.8)$$

where  $\mu$  and  $\lambda$  are new parameters that identify a mass term and a self-interaction term of the field  $\phi$ . The potential is symmetric under rotations in the  $\phi$  space and its shape depends on the sign of the two parameters. When considering  $\lambda > 0$  and  $\mu^2 < 0$ , a characteristic shape with a continuum of minima is obtained, as shown in Figure 1.2. Due to the form of the potential, the field is forced to select an arbitrary minimum that breaks the rotational (gauge) invariance. The conventional choice is  $\langle \phi_3 \rangle = v$  and  $\langle \phi_1 \rangle = \langle \phi_2 \rangle = \langle \phi_4 \rangle = 0$ , where  $v$  is a parameter with the dimension of an energy known as the vacuum expectation value of the Higgs field:

$$v \equiv \sqrt{\frac{-\mu^2}{\lambda}} \quad (1.9)$$

The above choice allows to write a perturbation of the field  $\phi$  around the minimum as

$$\phi = \frac{1}{\sqrt{2}} \begin{pmatrix} 0 \\ v + H(x) \end{pmatrix} \quad (1.10)$$

where three degrees of freedom are removed and the remaining one describes a scalar field with excitations around the vacuum expectation value  $v$ . If the expression 1.10 is used in the Lagrangian 1.6, the mass terms of the bosons appear from the expansion of the covariant derivative  $D_\mu$  coupled to the Higgs field, yielding:

$$m_W = \frac{gv}{2} \quad m_Z = \frac{v}{2} \sqrt{g^2 + g'^2} \quad m_A = 0 \quad (1.11)$$

where  $g$  and  $g'$  are the couplings strengths of the  $SU(2)_L$  and  $U(1)_Y$  groups, related to the Weinberg angle by

$$\sin(\theta_W) = \frac{g'}{\sqrt{g^2 + g'^2}} \quad (1.12)$$

It is interesting to notice that the spontaneous symmetry breaking mechanism is predicting a relation between the masses of  $W$  and  $Z$  bosons,  $m_W = m_Z \cos(\theta_W)$ , that is consistent with the experimental measurements.

Once the masses of the gauge bosons are established, the following step is to consider the case of the fermions. A mass term in its simplest form,  $m\bar{\psi}\psi = m(\bar{\psi}_L\psi_R + \bar{\psi}_R\psi_L)$ , is not gauge invariant because the left handed components of the fermions are  $SU(2)_L$  doublets while the right handed components are singlets, so they transform in a different way. The solution is to introduce the Higgs field in the term as

$$\mathcal{L}_f = -\lambda_f(\bar{\psi}_L\phi\psi_R + \bar{\psi}_R\bar{\phi}\psi_L) \quad (1.13)$$

where the gauge invariance is preserved thank to the presence of two  $SU(2)$  doublets. In the case of leptons doublets,  $(\nu_\ell, \ell)$ , the term can be rewritten using Higgs field expansion from Equation 1.10:

$$\begin{aligned} \mathcal{L}_\ell &= -\lambda_\ell \left[ (\bar{\nu}_\ell \bar{\ell})_L \begin{pmatrix} 0 \\ v + H \end{pmatrix} \ell_R + \bar{\ell}_R (0, v + H) \begin{pmatrix} \nu_\ell \\ \ell \end{pmatrix}_L \right] \\ &= -\frac{\lambda_\ell v}{\sqrt{2}} \bar{\ell} \ell - \frac{\lambda_\ell H}{\sqrt{2}} \bar{\ell} \ell = -m_\ell \bar{\ell} \ell - \frac{m_\ell}{v} H \bar{\ell} \ell \end{aligned} \quad (1.14)$$

where the two terms that appear describe the mass of the leptons and their interaction with the Higgs, both related to the vacuum expectation value  $v$  and the Yukawa couplings  $\lambda_\ell$ . Equation 1.13 can also be used for the masses of down-type quarks, but additional terms are needed for up-type quarks and possibly for neutrinos. The new terms can have the same structure of Equation 1.13, but they require the complex conjugate of the the Higgs field defined as

$$\phi_c \equiv -i\tau_2\phi^\star = -\frac{1}{\sqrt{2}} \begin{pmatrix} v + H \\ 0 \end{pmatrix}$$

In summary, the spontaneous symmetry breaking mechanism is based on the introduction of a new Higgs field with four degrees of freedom, shown in Equation 1.7. Three degrees of freedom are then used to generate the mass terms of the  $W^\pm$  and  $Z$  bosons, as a result of the choice of vacuum (Equation 1.10). The remaining one appears as a new scalar, the Higgs boson, with Yukawa couplings to the Standard Model particles and with

mass given by the quadratic term of the potential in Equation 1.8:

$$m_H^2 = 2\mu^2 = 2\lambda v^2 \quad (1.15)$$

### The observation of the Higgs boson

The discovery of a new scalar particle with mass around 125 GeV, compatible with the properties of the Higgs boson, was announced by the ATLAS [10] and CMS [11] Collaborations on July 4<sup>th</sup>, 2012. Since then the Higgs has been measured in multiple decay channels, yielding no significant deviation with respect to the Standard Model predictions. The mass is now known with a precision of about 0.2% [12, 13] and the signal strength in the different channels is consistent with the predictions for Yukawa couplings, as shown by the combined ATLAS and CMS summary plot in Figure 1.3. The couplings are compatible with a linear fit over several orders of magnitudes, providing strong evidence of the validity of the electroweak symmetry breaking mechanism. The precision of the measurements is limited by the capabilities of the LHC experiments, where some decay channels are particularly challenging due to the combination of low signal cross section and large backgrounds. Improving their accuracy is a major goal of the experimental community, because any deviation with respect to the predictions would indicate the presence of new physics beyond the Standard Model.

## 1.2 The limitations of the Standard Model

The Standard Model provides an accurate and self-consistent description of fundamental interactions, extensively tested in high energy physics experiments. Despite its major successes, however, there are several reasons to believe that the present theory is not complete. This section describes the most compelling issues that call for an extension of the Standard Model, highlighting the problems related to the Higgs mass scale and the absence of a dark matter candidate.

### 1.2.1 The Higgs hierarchy problem

A major problem of the Standard Model arises from the large difference between the scale of the Higgs boson mass,  $10^2$  GeV, and the Planck scale,  $10^{19}$  GeV, at which quantum gravity effects are expected to dominate with respect to the other interactions [15–17]. In the theory, the value of the Higgs boson mass can be computed as the sum of two components:

$$m_H^2 = m_{H_0}^2 + \delta m_H^2 \quad (1.16)$$

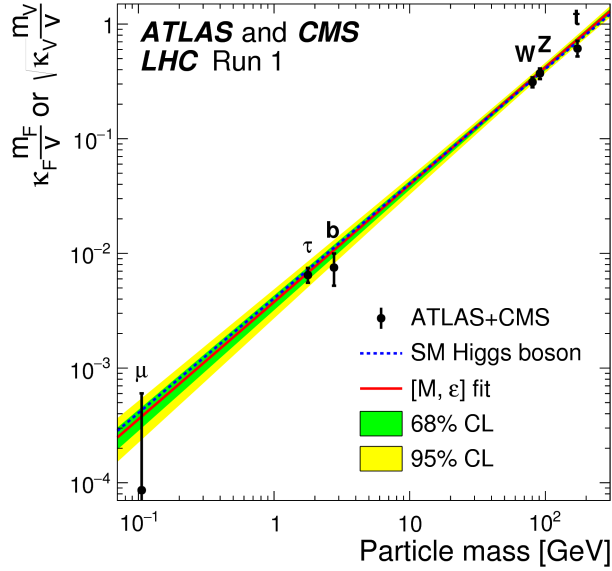


Figure 1.3: Strength of the Higgs boson couplings to the Standard Model particles as a function of their masses [14]. The linear fit shows that the measured values are consistent with the expectations within uncertainties.

where  $m_{H_0}$  is the bare mass, a free parameter of the Lagrangian, and  $\delta m_H$  is a radiative correction that depends on the Higgs couplings to other particles. Due to the structure of the Yukawa couplings, it is easy to show that a major correction is given by the diagram in Figure 1.4, where a fermion loop is added to the Higgs propagator. For a fermion with coupling  $\lambda_f$  the size of the correction is given by

$$\delta m_H^2|_f = -\frac{|\lambda_f|}{8\pi^2} \Lambda_{\text{NP}}^2 + \dots \quad (1.17)$$

where  $\Lambda_{\text{NP}}$  is the highest mass scale in the theory. Due to the quadratic dependence on  $\Lambda_{\text{NP}}$ , the correction  $\delta m_H$  is strongly sensitive to any particle with mass beyond the

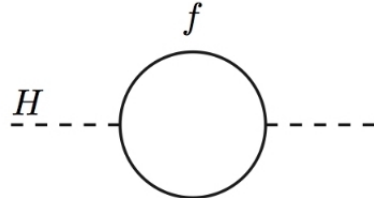


Figure 1.4: Fermion loop correction to the Higgs boson mass.

electroweak scale. In particular, the reasonable assumption that new physics exists at the Planck scale implies that  $\delta m_H$  is of the order of  $10^{19}$  GeV, pushing  $m_H$  far from the measured value of  $\sim 125$  GeV. The only way to predict the value of  $m_H$  at the electroweak scale is to fine tune the bare parameter  $m_{H_0}$  in Equation 1.16 such that it almost perfectly cancels the large radiative correction. The Higgs mass is thus obtained as the difference between two terms of  $10^{19}$  GeV each.

The large discrepancy between the measured scale of the Higgs boson mass and the Planck scale is known as the Higgs hierarchy problem. The Standard Model solution based on the tuning of  $m_{H_0}$  is in contrast with the argument of naturalness, according to which these fine cancellations should not occur unless they arise from a specific feature of the theory. For example, the light masses of fermions and vector bosons are not concerning because their value is protected by chiral and gauge symmetries, which imply that any radiative correction can only be proportional the mass itself ( $\delta m_\psi \propto m_\psi$  and  $\delta A^2 \propto A^2$ ). The case of the scalar Higgs boson is special because no symmetry is protecting the mass, which can then receive larger corrections as the one in Equation 1.17. A possible solution to the problem is to postulate the existence of an extra symmetry that provides a natural explanation to the discrepancy between the electroweak and Planck scales. This is what happens in supersymmetric extension of the Standard Model, as described in Section 1.3.3.

### 1.2.2 Dark matter

Astrophysical observations have identified a variety of systems where the amount of ordinary matter, estimated through the light that it emits, is incompatible with the gravitational pattern. These results suggest the presence of an extra type of matter, dark matter, that must contribute to the gravitational effects without yielding any extra luminosity [18]. To do so, dark matter particles need to be metastable or stable, massive, weakly interacting and electrically neutral. Since none of the Standard Model particles satisfy these criteria, the evidence of dark matter is a clear indication that the present theory is incomplete.

Searches for dark matter can be conducted in different ways, including collider experiments where the new particles may be produced in the final states of exotic physics processes. As described in Section 1.3, supersymmetric theories can embed dark matter candidates in many different ways, making them extremely interesting to search for at the LHC.

### 1.2.3 More open issues

Along with the hierarchy problem and the absence of a dark matter candidate, there is more evidence that motivates the need for physics beyond the Standard Model. In the list below I briefly discuss some open issues that are being addressed by the scientific community:

- *Grand Unification*: Following the success of the electroweak theory, where weak force and electromagnetism are successfully described as the low energy limit of a single interaction, theorists have been exploring the possibility of a further unification that incorporates also the strong force. For this purpose, it is necessary to examine the evolution (*running*) of the coupling constants of each Standard Model interaction as a function of the energy scale [19]. As seen in Section 1.1.2 in the case of  $\alpha_s$  (Equation 1.5), the value of the constants has a non-trivial dependence on the energy scale determined by the number of degrees of freedom of the theory. In the Standard Model, the evolution of the coupling constants of electromagnetic, weak and strong interactions is not converging to a common value, as shown by Figure 1.5a. This is in contrast with the idea of a unification of the interactions, that requires a unique coupling strength at a Grand Unification scale  $\mu_{\text{GUT}}$ . The necessary behaviour can be recovered by introducing Supersymmetry, which varies the particle content of the theory and modifies the scale dependence of the constants such that the three curves can intersect (Figure 1.5b).
- *Neutrino sector*: The Standard Model predicts the existence of three types of massless neutrinos that can only convert into their corresponding charged lepton via electroweak interactions. However, the recent discovery of neutrino oscillations violates lepton flavour conservation and indicates that at least two of the three species must have non-zero mass [21]. Both these properties imply that the neutrino sector of the Standard Model is not complete, calling for a deeper understanding of the underlying physics.
- *CP violation*: In the Standard Model the only measured source of CP violation is a complex phase in the CKM matrix [22], which is not sufficient to explain the relative abundance of matter and antimatter in the universe [23]. In order to solve this puzzle, additional sources of CP violation are expected to appear in new physics scenarios.
- *Gravity*: As previously discussed in this chapter, no description of gravity is included in the Standard Model. The development of a quantum description of grav-

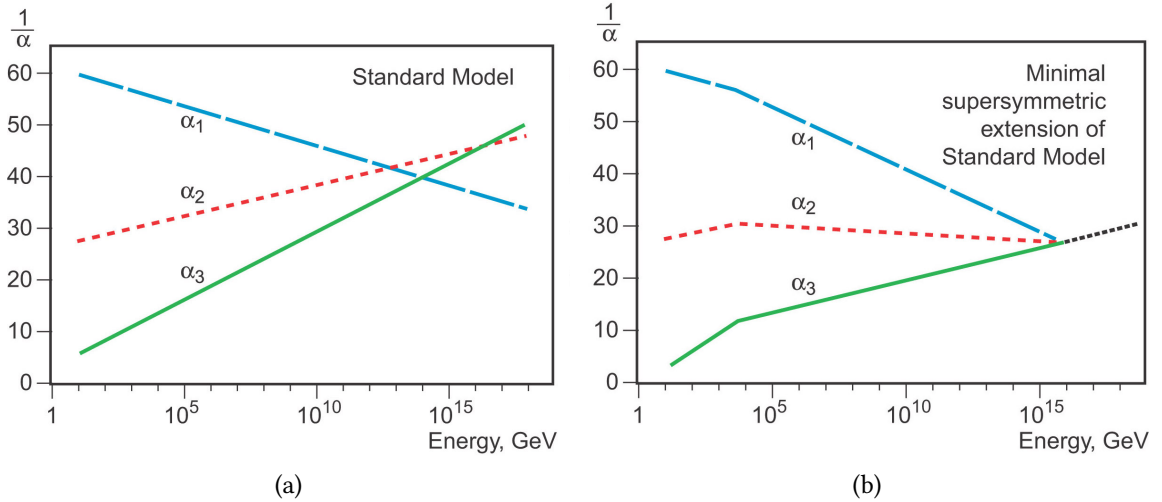


Figure 1.5: Evolution of the coupling constants of electromagnetic, weak and strong interactions as a function of energy in the Standard Model (a) and in a supersymmetric extension (b) [20].

ity is an ultimate goal of the scientific community.

### 1.3 Supersymmetry

This section provides an introduction to supersymmetric extensions of the Standard Model [24, 25], showing that they can solve many of the outstanding issues in high energy physics. The section begins with a theoretical introduction to supersymmetric Lagrangians, while in the second part the Minimal Supersymmetric Standard Model (MSSM) is introduced, highlighting the classes of models that are most relevant for this thesis.

#### 1.3.1 Supersymmetric theories

Supersymmetry (SUSY) is a type of spacetime symmetry that extends the Poincaré group of the Standard Model with a new transformation between bosonic and fermionic states. In the Standard Model two distinct types of symmetry are implemented:

- *Spacetime symmetries*, that form the Poincaré group and cause the conservation of four-momentum and angular momentum.

- *Gauge symmetries* or *local symmetries*, that result in the conservation of the associated charges.

A fundamental theorem by Coleman and Mandula [26] states that local and spacetime symmetries can only be combined as direct products, as it happens in the Standard Model, otherwise the theory would be unable to predict scattering amplitudes with non-zero probability. This seems to imply that there is no way to introduce new hybrid types of symmetries, because the interactions between the fields would no longer be described. However, it can be shown that the Coleman-Mandula theorem does not apply to symmetries generated by fermionic transformations, where an operator  $Q$  acts on a state and modifies its spin by  $\frac{1}{2}$ . These special types of symmetries are known as supersymmetries, and the corresponding transformations are given by:

$$\begin{aligned} Q |\text{boson}\rangle &= |\text{fermion}\rangle \\ Q |\text{fermion}\rangle &= |\text{boson}\rangle \end{aligned} \quad (1.18)$$

The spin difference between the initial and final state of the transformation implies that the operator  $Q$  must be a spin- $\frac{1}{2}$  object. If we let  $Q_\alpha$  ( $\alpha = 1, 2$ ) and  $Q_\beta^\dagger$  be the components of the generator  $Q$  and of its hermitian conjugate  $Q^\dagger$ , their anticommutator is given by

$$\{Q_\alpha, Q_\beta^\dagger\} = 2\gamma_{\alpha\beta}^\mu p_\mu \quad (1.19)$$

where  $p_\mu$  is the Lorentz four-momentum and  $\gamma^\mu$  are the Dirac matrices. Other important commutators are:

$$\begin{aligned} [M^{\rho\sigma}, Q_\alpha] &= -i(\sigma^{\rho\sigma})_\alpha^\beta Q_\beta \\ \{Q_\alpha, Q_\beta\} &= \{Q_\alpha^\dagger, Q_\beta^\dagger\} = 0 \\ [p^\mu, Q_\alpha] &= [p^\mu, Q_\alpha^\dagger] = 0 \end{aligned} \quad (1.20)$$

where  $M^{\rho\sigma}$  is the generator of the Lorentz transformations. From the last line it can be seen that the generator  $Q$  commutes with  $p^2 = m^2$ , which implies that fermion-boson pairs related by the transformation have the same mass. In supersymmetric extensions of the Standard Model the commutators of  $Q$  with the generators of the gauge transformations must also vanish, in order to preserve the existing structure of the theory. Fermions and bosons related by  $Q$  must then have the same  $SU(3)_C \otimes SU(2)_L \otimes U(1)_Y$  quantum numbers, which is not the case for any pair of particles in the Standard Model, indicating that none of the known objects can be regarded as the superpartner of any other. Since supersymmetry needs to apply to all fields in the theory, it follows that minimal extensions of the Standard Model require the introduction of a new superpartner for each particle, incrementing the number of elementary states by at least a factor 2.

## Superfields

The Standard Model particles and their superpartners are organised in supermultiplets that contain two bosonic and two fermionic degrees of freedom. The fermions are described by Weyl spinors [27] with two polarisations, and for each of them there is a corresponding bosonic state. When the operators  $Q$  and  $Q^\dagger$  act on the supermultiplets, they transform the bosonic components into the fermionic ones and vice versa. Depending on the spin of the particles involved, the supermultiplets can be classified as follows:

- *Chiral supermultiplets* contain spin- $\frac{1}{2}$  fermions with left and right handed components,  $f_L$  and  $f_R$ , and two spin-0 partners known as scalar fermions or sfermions. The two scalars are conventionally labelled  $\tilde{f}_L$  and  $\tilde{f}_R$ , where the tilde is used to identify SUSY particles and the  $L$  and  $R$  labels are referred to the chirality of the partners.
- *Gauge supermultiplets* contain vector bosons, assumed to be massless, and two spin- $\frac{1}{2}$  Weyl fermions known as gauginos.
- *Gravitational supermultiplets* include the spin-2 graviton and a spin- $\frac{3}{2}$  partner, the gravitino.

### 1.3.2 The Minimal Supersymmetric Standard Model (MSSM)

This paragraph describes the simplest supersymmetric extension of the Standard Model, known as Minimal Supersymmetric Standard Model (MSSM), where a new superpartner is added for each standard particle. The MSSM preserves the  $SU(3)_C \otimes SU(2)_L \otimes U(1)_Y$  gauge symmetry of the Lagrangian, so the quantum numbers of particles and superpartners are the same. The field content of the theory is the following:

- A chiral supermultiplet  $q_{L,R}-\tilde{q}_{L,R}$  for each quark in the Standard Model.
- A chiral supermultiplet  $\ell_{L,R}-\tilde{\ell}_{L,R}$  for each lepton family.
- A gauge supermultiplet for each vector boson in the Standard Model and its spin- $\frac{1}{2}$  partner:  $B_0-\tilde{B}_0, W_i-\tilde{W}_i, g-\tilde{g}$ .
- Two chiral supermultiplets,  $H_u-\tilde{H}_u$  and  $H_d-\tilde{H}_d$ , that embed the Standard Model Higgs and give mass to bosons and fermions through the usual spontaneous symmetry breaking mechanism. Among the total of eight degrees of freedom only three are involved in the symmetry breaking, so the remaining five can appear as observable states:

- $H^\pm$ : two charged Higgs states.
- $A^0$ : a CP-odd neutral Higgs.
- $h^0$  and  $H^0$ : two neutral CP-even Higgs fields, one of which must be the Standard Model Higgs boson.

### SUSY Lagrangian and $R$ -parity

Once the field content is defined it is possible to examine the most general expression of the SUSY Lagrangian, that contains a larger number of terms with respect to the Standard Model. Some of these terms violate the conservation of lepton and baryon number, which is instead prohibited in the Standard Model, so they enable processes like proton decay that are heavily constrained by experimental data. In order to remove them from the SUSY Lagrangian, a solution is to introduce a new quantum number known as  $R$ -parity [28] that can be expressed as a function of baryon and lepton numbers,  $B$  and  $L$ , and of the spin  $S$ :

$$P_R \equiv (-1)^{3(B-L)+2S}. \quad (1.21)$$

With the above definition,  $R$ -parity provides a simple classification of the particles:

- Standard Model particles  $\rightarrow P_R = 1$
- SUSY particles  $\rightarrow P_R = -1$

In SUSY models where  $R$ -Parity is conserved, the Lagrangian terms that violate lepton and baryon number are automatically forbidden. The structure of the remaining terms implies that any Feynman diagram must only include vertices with an even number of SUSY particles, with relevant consequences on the phenomenology:

- SUSY particles must be produced in pairs.
- The decay of a SUSY particle must contain an odd number of SUSY particles.
- The Lightest Supersymmetric Particle (LSP) must be stable.

### SUSY breaking

As seen in Section 1.3.1, supersymmetric extensions of the Standard Model require that particles and superpartners are mass-degenerate. This is clearly incompatible with the experimental data, because so far no evidence of SUSY particles has been found. The lack of observations indicates that SUSY, if it exist, must be broken in a way that makes

the superpartners significantly heavier than the Standard Model particles.

In the absence of experimental hints, the mechanism responsible for SUSY breaking can only be guessed based of generic arguments. As discussed in Ref. [29], a spontaneous breaking is not possible within the framework of the MSSM without the introduction of at least one extra field, with little or no indication about its properties. For this reason, a standard approach is to keep the field content of the theory to the minimum and introduce extra terms that break the symmetry explicitly, obtaining a Lagrangian of the form:

$$\mathcal{L} = \mathcal{L}_{\text{SUSY}} + \mathcal{L}_{\text{soft}} \quad (1.22)$$

where the *soft* label indicates that the new terms must not spoil the renormalisability of the theory, and should be regarded as a perturbation of the supersymmetric part of the Lagrangian. In practice, the soft term is parametrising our ignorance about the exact mechanism responsible for the SUSY breaking, describing its consequences without specifying its origin. The inclusion of the soft term increases the number of free parameters of the theory to 105 in addition to the ones of the Standard Model. The phenomenology is strongly dependent on them, so it is common to classify the different models based on assumptions about their values.

### Mass eigenstates

As a result of the SUSY breaking, the masses of the superpartners become free parameters and can be different from those of the Standard Model particles. SUSY particles with the same quantum numbers can also mix, so the mass eigenstates are not necessarily the same as the interaction eigenstates introduced in the previous paragraph. The list below provides an overview of the mass eigenstates in the MSSM, that are also summarised in Table 1.1:

**Sleptons and squarks** Contrarily to what happens for standard particles, the left and right handed superpartners of quarks and leptons are not constrained to have equal mass. It is hence possible to define a mixing matrix that rotates the interactions eigenstates  $\tilde{q}_L$ - $\tilde{q}_R$  into mass eigenstates  $\tilde{q}_1$ - $\tilde{q}_2$ , where by convention  $\tilde{q}_1$  is the lightest. The structure of the mixing matrices is similar for squark and sleptons, and its expression in the case of third generation squarks [30] is given by:

$$\mathcal{M}_{\tilde{q}}^2 = \begin{pmatrix} m_{\tilde{q}_L}^2 & a_q m_q \\ a_q m_q & m_{\tilde{q}_R}^2 \end{pmatrix} \quad (1.23)$$

with

$$m_{\tilde{q}_L}^2 = M_{Q_3}^2 + m_Z^2 \cos 2\beta (I_3^{q_L} - e_q \sin^2 \theta_W) + m_q^2, \quad (1.24)$$

$$m_{\tilde{q}_R}^2 = M_{\{U,D\}_3}^2 + m_Z^2 \cos 2\beta e_q \sin^2 \theta_W + m_q^2, \quad (1.25)$$

$$a_q m_q = \begin{cases} (A_t - \mu \cot \beta) m_t & (\tilde{q} = \tilde{t}) \\ (A_b - \mu \tan \beta) m_b & (\tilde{q} = \tilde{b}) \end{cases} \quad (1.26)$$

In the above equations  $I_3^q$  is the third component of the weak isospin,  $e_q$  the fractional electric charge of the quark  $q$  and  $m_Z$  is the mass of the Standard Model  $Z$  boson. In addition,  $\mu$  is the higgsino mass parameter in the MSSM and  $\tan \beta$  is the ratio between the vacuum expectation values of  $H_u$  and  $H_d$ . The remaining parameters are introduced in  $\mathcal{L}_{\text{soft}}$ :  $M_{Q_3, U_3, D_3}$  are the third components of the mass matrices of left and right handed squarks, corresponding to the third generation, while  $A_{t,b}$  are the coefficients of their trilinear coupling terms. The impact of the mixing is particularly relevant for the partners of the heavy flavour families, stop ( $\tilde{t}_{1,2}$ ) and sbottom ( $\tilde{b}_{1,2}$ ), due to the presence of the mass of the Standard Model fermions in the off-diagonal terms of the matrix.

**Gluinos** Since gluons and gluinos carry colour charge, no mixing can occur and the mass eigenstates correspond to the interaction eigenstates.

**Neutralinos and charginos** The charged Higgs states mix with the superpartners of the gauge bosons, the gauginos, yielding two pairs of positively or negatively charged spin- $\frac{1}{2}$  mass eigenstates known as charginos,  $\tilde{\chi}^\pm$ . The mixing matrix is

$$\begin{pmatrix} M_2 & \sqrt{2}m_W \sin \beta \\ \sqrt{2}m_W \cos \beta & \mu \end{pmatrix} \quad (1.27)$$

in the  $(W^\pm, H^\pm)$  basis, where  $M_1$  and  $M_2$  are gaugino mass parameters from  $\mathcal{L}_{\text{soft}}$ ,  $m_W$  is the mass of the  $W$  boson, and  $\beta$  and  $\mu$  are defined as in Equations 1.23-1.26. In a similar way, four neutral spin- $\frac{1}{2}$  particles called neutralinos ( $\tilde{\chi}_i^0$  with  $i = 1, 2, 3, 4$ ) result from the mixing of the charge-neutral interaction eigenstates from the Higgs and gauge sectors. The  $4 \times 4$  mixing matrix in the  $(B, W^0, H_d, H_u)$  basis is

$$\begin{pmatrix} M_1 & 0 & -m_Z \cos \beta \sin \theta_W & m_Z \sin \beta \sin \theta_W \\ 0 & M_2 & m_Z \cos \beta \cos \theta_W & m_Z \sin \beta \cos \theta_W \\ -m_Z \cos \beta \sin \theta_W & m_Z \cos \beta \cos \theta_W & 0 & \mu \\ m_Z \sin \beta \sin \theta_W & -m_Z \sin \beta \cos \theta_W & -\mu & 0 \end{pmatrix} \quad (1.28)$$

Names	Spin	$P_R$	Gauge Eigenstates	Mass Eigenstates
Higgs bosons	0	+1	$H_u^0 \ H_d^0 \ H_u^+ \ H_d^-$	$h^0 \ H^0 \ A^0 \ H^\pm$
squarks	0	-1	$\tilde{u}_L \ \tilde{u}_R \ \tilde{d}_L \ \tilde{d}_R$ $\tilde{s}_L \ \tilde{s}_R \ \tilde{c}_L \ \tilde{c}_R$ $\tilde{t}_L \ \tilde{t}_R \ \tilde{b}_L \ \tilde{b}_R$	(same) (same) $\tilde{t}_1 \ \tilde{t}_2 \ \tilde{b}_1 \ \tilde{b}_2$
sleptons	0	-1	$\tilde{e}_L \ \tilde{e}_R \ \tilde{\nu}_e$ $\tilde{\mu}_L \ \tilde{\mu}_R \ \tilde{\nu}_\mu$ $\tilde{\tau}_L \ \tilde{\tau}_R \ \tilde{\nu}_\tau$	(same) (same) $\tilde{\tau}_1 \ \tilde{\tau}_2 \ \tilde{\nu}_\tau$
neutralinos	1/2	-1	$\tilde{B}^0 \ \tilde{W}^0 \ \tilde{H}_u^0 \ \tilde{H}_d^0$	$\tilde{N}_1 \ \tilde{N}_2 \ \tilde{N}_3 \ \tilde{N}_4$
charginos	1/2	-1	$\tilde{W}^\pm \ \tilde{H}_u^\pm \ \tilde{H}_d^\pm$	$\tilde{C}_1^\pm \ \tilde{C}_2^\pm$
gluino	1/2	-1	$\tilde{g}$	(same)

Table 1.1: Particle content of the Minimal Supersymmetric Standard Model [31].

where the same parameters of the previously defined matrices are appearing.

### Phenomenological MSSM

The number of free parameters in the MSSM after SUSY breaking can be reduced under the following assumptions:

- The only source of CP violation in the theory is the Cabibbo-Kobayashi-Maskawa (CKM) matrix.
- No flavour changing neutral currents exist at tree level, implying that the sfermion mass matrices and trilinear coupling matrices must be diagonal.
- Universality applies to the first and second generation of the sfermions, whose masses are assumed to be degenerate.

As a result, the free parameters of the theory can be reduced to 19: the ratio  $\tan \beta$  between the VEVs of the two Higgs doublets, the mass of the pseudoscalar Higgs  $M_A$ , the Higgs-Higgsino mass parameter  $\mu$ , five mass parameters for 1<sup>st</sup> and 2<sup>nd</sup> generation sfermions and five more for 3<sup>rd</sup> generation sfermions, three mass parameters for gluino, Bino and Wino and three more parameters for third generation trilinear couplings. This simplified version of the theory is known as phenomenological Minimal Supersymmetric Standard Model, pMSSM.

### 1.3.3 SUSY as a solution to the hierarchy problem

The MSSM can address many of the outstanding issues of the Standard Model, including the Higgs hierarchy problem [32]. As discussed in Section 1.2.1, the problem originates from the divergent radiative corrections to the Higgs mass shown in Figure 1.4, that make the value of  $m_H$  extremely sensitive to any new physics at high energy scales. Supersymmetry introduces additional loops [31] involving the scalar partners of the fermions, as the one in Figure 1.6, so an extra radiative correction appears for both right and left handed superpartners:

$$\delta m_H^2|_s = + \frac{|\lambda_s|}{16\pi^2} \Lambda_{\text{NP}}^2 + \dots \quad (1.29)$$

where  $\lambda_s \equiv \lambda_f$  is the Yukawa coupling of the sfermions to the Higgs. Thanks to the fact that the couplings are the same, the two scalar contributions cancel exactly the divergent correction caused by the fermion loop, whose expression is defined in Equation 1.17. This implies that even hypothetical fermions with mass of the order of the Planck scale would not have an impact on the Higgs mass, so the measured value  $m_H \sim 125$  GeV can be obtained without any unnatural tuning of the parameters. In other words, supersymmetry is forcing  $\lambda_f$  and  $\lambda_s$  to be the same and, by doing so, it is removing the quadratic divergence in  $\Lambda_{\text{NP}}$ .

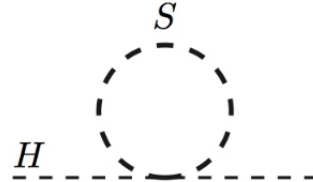


Figure 1.6: Scalar loop correction to the Higgs mass that cancels the fermion loop in Figure 1.4.

At higher order in perturbation theory, it can be shown that both fermions and scalars coupled to the Higgs yield corrections of the form:

$$\delta m_H^2|_X = \pm \frac{\lambda_X}{16\pi^2} m_X^2 \log \left( \frac{\Lambda_{\text{NP}}}{m_X^2} \right) + \dots, \quad X = f, s \quad (1.30)$$

where there  $\Lambda_{\text{NP}}$  appears in a logarithm but a quadratic dependence on the mass is introduced, and the sign is again opposite for scalars and fermions. In realistic models where SUSY is broken the above terms do not cancel, yielding a non-zero correction to the Higgs mass due to the mass difference between the standard particles and their

partners:

$$\delta m_H^2|_{s+f} = \frac{\lambda}{16\pi^2} \left[ m_f^2 \log \left( \frac{\Lambda_{\text{NP}}}{m_f^2} \right) - m_s^2 \log \left( \frac{\Lambda_{\text{NP}}}{m_s^2} \right) \right] \quad (1.31)$$

In order to keep the size of the correction under control, the difference between the masses of standard and SUSY particles with large couplings  $\lambda$  to the Higgs must not be too large. The exact threshold on the mass difference is arbitrary, and is determined by the amount of fine tuning that one is willing to accept without regarding the model as unnatural.

In the case of the top quark and its partner, the stop ( $\tilde{t}$ ), the correction in Equation 1.31 can be expressed as a function of the parameters of  $\mathcal{L}_{\text{soft}}$  [33]:

$$\delta m_H^2|_{stop} \simeq -\frac{3y_t^2}{8\pi^2} (m_{Q_3}^2 + m_{U_3}^2 + |A_t|^2) \log \left( \frac{\Lambda_{\text{NP}}}{\text{TeV}} \right) \quad (1.32)$$

where  $m_{Q_3}$  and  $m_{U_3}$  are the third components of the mass matrices of left and right squarks and the trilinear coupling coefficient, as introduced in Equations 1.23-1.26, and the dependence on the mass in the logarithm is neglected.

In the MSSM, an even stronger constraint is placed on the Higgsino mass parameter  $\mu$ , which is related to the Higgs mass at tree level and therefore should be close to the measured value of  $m_H$ :

$$\frac{m_H^2}{2} = -|\mu|^2 + \dots + \delta m_H^2 \quad (1.33)$$

Finally, the gluino mass parameter  $M_3$  is also constrained because it enters a 2-loop correction to the Higgs mass at 2-loop level:

$$\delta m_H^2|_{gluino} \simeq -\frac{2y_t^2}{\pi^2} \left( \frac{\alpha_s}{\pi} \right) |M_3|^2 \log^2 \left( \frac{\Lambda_{\text{NP}}}{\text{TeV}} \right) \quad (1.34)$$

The above arguments can be used to classify the mass eigenstates of the pMSSM. Higgsinos, third generation squarks and gluinos form the natural SUSY spectrum, while the rest of the sparticles can in principle be heavier without spoiling the naturalness of the theory, so they are referred to as decoupled SUSY.

The full spectrum of a natural pMSSM model is shown in Figure 1.7. If the  $\mu$  parameter in the mixing matrices of charginos and neutralinos (Equations 1.27-1.28) is assumed to be significantly smaller than the others, three light Higgsino-like mass eigenstates are predicted. Due to the structure of the squark mixing matrix (Equation 1.23) the constraints on  $m_{Q_3}$   $m_{U_3}$  imply that the left handed third generation squarks and the right handed  $\tilde{t}$  must also be light, with favoured decays into Standard Model top or bottom quarks plus one of the three Higgsinos. Gluinos are light because of the constraint on  $M_3$ , while the lightest Higgsino is assumed to be the LSP and provides a good candidate for dark matter.

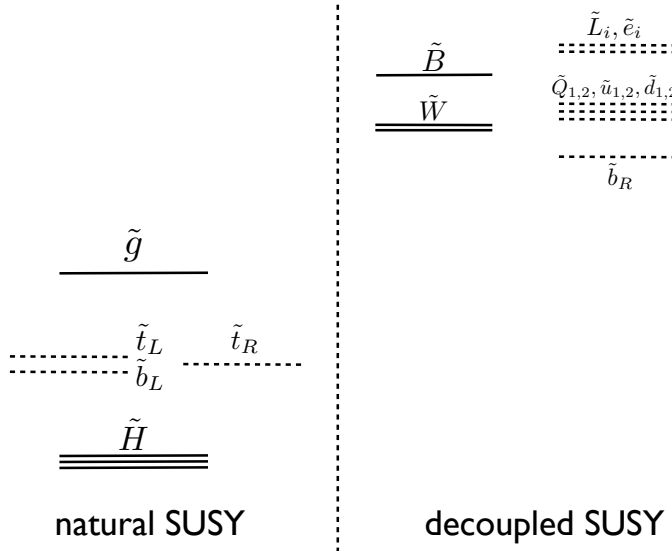


Figure 1.7: Natural pMSSM mass spectrum [33]. The particles on the left side are constrained by naturalness arguments, while the remaining ones are decoupled.

### 1.3.4 SUSY models with spontaneous $R$ -parity breaking

The imposition of  $R$ -parity, as described in Section 1.3.2, is an *ad-hoc* adjustment to the theory which is needed to remove unwanted terms from the Lagrangian. A formal way to embed it in the MSSM is to enlarge the gauge symmetry group to  $SU(3)_C \otimes SU(2)_L \otimes U(1)_Y \otimes U(1)_{B-L}$ , where the additional  $U(1)_{B-L}$  group naturally includes  $R$ -parity conservation. The caveat is that the  $U(1)_{B-L}$  symmetry is not observed at the electroweak scale, so a breaking mechanism must be assumed and RPV terms can appear as a consequence.

A minimal way to break  $U(1)_{B-L}$  spontaneously, without spoiling experimental constraints such as the limits on the proton decay, is to assume that right-handed scalar neutrinos (sneutrinos) develop a non-zero vacuum expectation value (VEV) [34]. This gives rise to a class of models that can be referred to as minimal  $B - L$  MSSM, with at least three major phenomenological features:

- The introduction of RPV terms implies that the Lightest Supersymmetric Particle (LSP) can carry colour or electric charge without causing a conflict with astrophysical data, because a prompt decay into Standard Model particles is possible.
- Since the spontaneous breaking of  $U(1)_{B-L}$  happens through the VEV of right

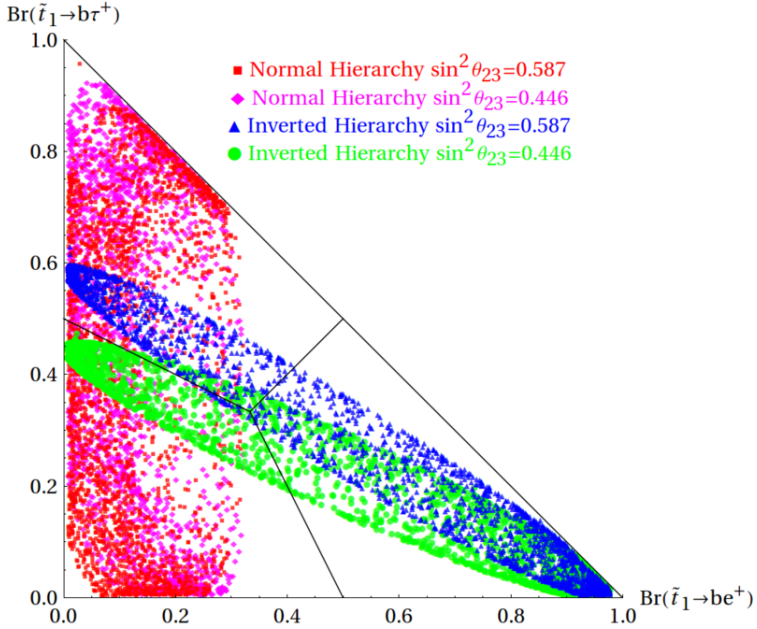


Figure 1.8: Scan of the branching ratio of the stop decay into  $b-e$ ,  $b-\mu$  and  $b-\tau$  as a function of free parameters of the minimal  $B-L$  MSSM, for a fixed mass hierarchy and for a fixed value of  $\sin^2(\theta_{23})$ . The scan parameters in the plot include the mass of the  $\tilde{t}_1$ , ranging from 400 GeV to 1 TeV. The values of  $\sin^2(\theta_{23})$  are taken from NuFIT-v1.2 [35].

handed neutrinos, the branching ratio of the LSP decays can be directly related to the neutrino mass hierarchy and to the value of the mixing angle  $\theta_{23}$ .

- Once the LSP is chosen, its decays are fixed by the theory as a result of the coupling structure of the minimal MSSM.

The nature of the LSP is not determined by the properties of the minimal  $B-L$  MSSM, but the distinctive trait of the theory is that it allows such particle to be colour charged. It can be shown that gluinos cannot be LSPs without spoiling the unification of gauge coupling parameters, so the most interesting LSP candidates to examine are the squarks. Moreover, third generation squarks are well motivated to be lighter than the others, so it is reasonable to focus the attention on the stop and sbottom. Considering the case of the stop, the decay is determined by the structure of the MSSM couplings:

$$\tilde{t}_1 \rightarrow b\ell, \quad \ell = e, \mu, \tau \quad (1.35)$$

and the branching ratios into electrons, muons and  $\tau$  leptons depend on the many parameters of the theory.

As anticipated, it is possible to correlate the branching ratio of the stop decay with the

neutrino mass hierarchy and the mixing parameter  $\sin^2(\theta_{23})$ . Figure 1.8 from Ref. [34] shows a full scan of the branching ratios in the  $\text{BR}(e)$ - $\text{BR}(\tau)$  plane as a function of the free parameters of the theory, for given neutrino mass hierarchies and for  $\sin^2(\theta_{23}) = 0.446$  or  $\sin^2(\theta_{23}) = 0.587$ . Interestingly, this implies that the experimental measurement of the branching ratio of a stop LSP within the minimal  $B - L$  MSSM would provide useful information to discriminate between the neutrino mass hierarchies and the two possible values of  $\sin^2(\theta_{23})$ .

## 1.4 SUSY searches at the LHC

The core topic of this thesis is the search for third generation squarks with the ATLAS detector, where SUSY particles are expected to appear in proton-proton collisions produced by the LHC at  $\sqrt{s} = 13$  TeV. This section provides an overview of the typical approach to the physics analyses, highlighting the challenges that they pose and the strategies used to overcome them. Various possible experimental signatures of third generation squarks are also discussed.

### 1.4.1 Experimental challenges and benchmark models

The production of the most relevant SUSY processes at the LHC is regulated by  $R$ -parity conserving couplings, with model-dependent exceptions far beyond the scope of this thesis. As a consequence, the physics analyses are done under the assumption that SUSY particles are pair-produced.

Figure 1.9 shows the cross section of the main processes [36] obtained by treating squarks and gluinos as decoupled particles, which means that squarks do not contribute to gluino production diagrams and vice versa. Under this assumption, the cross section of squark pair-production is found to be the same for all families, with a twofold degeneracy for each flavour due to the presence of left and right handed components. Gluinos have a relatively large cross-section, while neutralinos and charginos are disfavoured because their production is mediated by electroweak interaction. For reference, the cross sections of various Standard Model processes measured by ATLAS at  $\sqrt{s} = 7, 8$  and  $13$  TeV are shown in Figure 1.10. Any search for SUSY particles must separate the signal of interest from an overwhelming amount of background, whose rate is larger by several orders of magnitude.

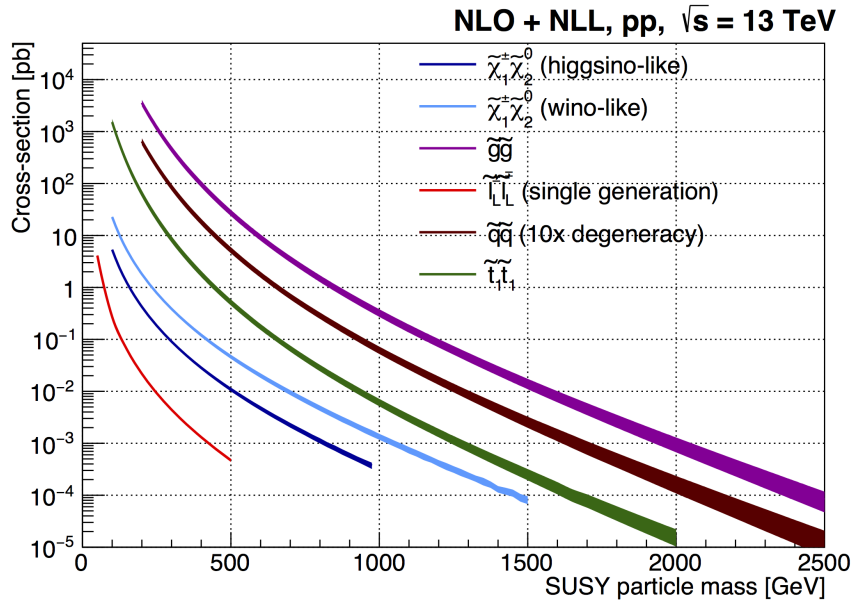


Figure 1.9: Cross sections for pair production of SUSY particles as a function of their mass in proton-proton collisions at  $\sqrt{s} = 13 \text{ TeV}$ . The cross sections are computed under the assumption that the different SUSY particles are decoupled.

### Simplified models

The parametrisation of SUSY benchmark models can be quite challenging from a practical point of view, due to the large number of particles and degrees of freedom in the MSSM. A common strategy [37] is to concentrate on specific signal processes extracted from the full models, ignoring any particle that does not contribute to them. For example, an analysis can be designed to target the two-body decay of a pair-produced third generation squark into two bottom quarks and two neutralinos, neglecting completely the rest of the SUSY mass spectrum. This signature-based approach allows to minimise the number of free parameters that define the phenomenological properties of the signal: in the above example, the masses of squarks and neutralinos are sufficient. When using simplified models it is important to keep track of the broader theoretical framework where they are embedded, but due to their convenience they have become a standard tool for SUSY searches. The simplicity of the signal benchmarks also benefits the reinterpretation of the results of the analyses under different theoretical assumptions, a powerful way to constrain new models. All the analyses presented in this thesis are based on simplified models, motivated by the theoretical arguments discussed in this chapter.

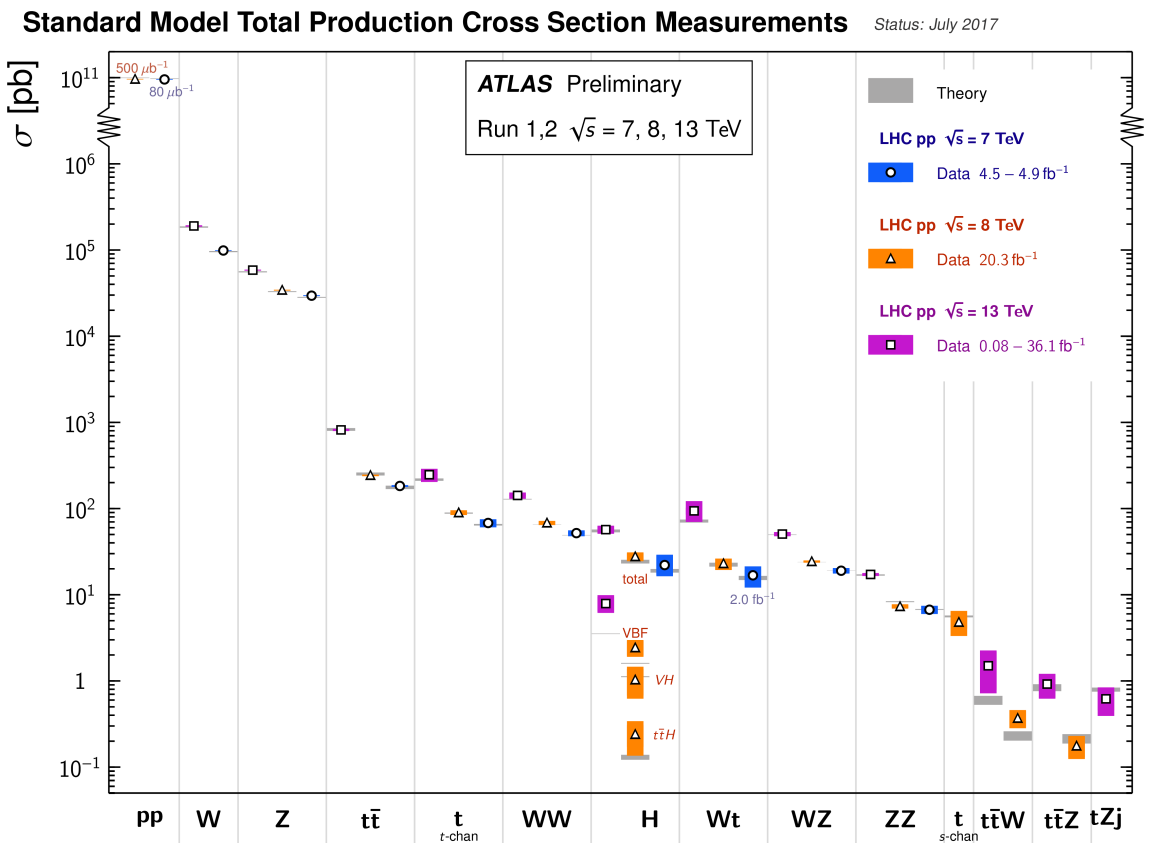


Figure 1.10: Summary of the cross sections of the most relevant Standard Model processes measured by the ATLAS experiment at  $\sqrt{s} = 7, 8$  and  $13$  TeV.

### 1.4.2 Phenomenology of third generation squarks

The cross section of stop and sbottom pair-production with decoupled gluinos depends only on the mass of the sparticles, but the experimental signature of the models varies significantly if different decays are considered. While lighter signals are generally easier to target thanks to the larger production rate, in some situations the kinematic properties of the final states resemble those of the Standard Model backgrounds, compromising the possibility to obtain an effective separation. For each SUSY particle, it is hence important to prepare dedicated analysis strategies for different hypotheses on masses and decay modes. In the case of third generation squarks, the experimental signatures are generally similar for stop and sbottom production, so the analyses can often be interpreted in both scenarios. The next pages provide an overview of the phenomenology studied by the ATLAS Collaboration, highlighting the differences between the two cases.

#### *R*-parity conserving decays

The ATLAS searches for stop or sbottom pair-production with RPC decays are usually done under the assumption of a neutralino ( $\tilde{\chi}_1^0$ ) LSP [38]. This choice satisfies the requirements of the natural pMSSM spectrum shown in Figure 1.7 and provides a good candidate for dark matter. In the simplest case the squarks decay directly into the LSP plus some extra Standard Model particles, so the signal properties are basically defined by fixing the values of the masses of the two superpartners. More degrees of freedom appear if additional SUSY particles are included in the decay chain, such as heavier neutralinos or charginos.

The signal benchmark samples are typically generated as a grid of simplified models parametrised by the mass of the third generation squark and of one of the SUSY particles from the decay chain. If more than two SUSY particles are involved, dedicated assumptions are made on the masses of the extra ones in order to keep a total of two free parameters. For example, when working in the framework of the natural pMSSM spectrum it is necessary to include an extra light chargino ( $\tilde{\chi}_1^+$ ) and a next-to-lightest neutralino ( $\tilde{\chi}_2^0$ ) in addition to the  $\tilde{t}$  (or  $\tilde{b}$ ) and the  $\tilde{\chi}_1^0$ . A two-dimensional signal grid can be obtained by making an assumption on the mass splitting between the heavier Higgsinos and the LSP, leaving the values of  $m_{\tilde{t}}$  and  $m_{\tilde{\chi}_1^0}$  as the only free parameters.

The most relevant decay modes of the  $\tilde{t}$  that terminate with the production of a  $\tilde{\chi}_1^0$  are shown in Figure 1.11 in the  $m_{\tilde{t}}\text{-}m_{\tilde{\chi}_1^0}$  plane. The dominant final states are different depending on which region of the parameter space is considered, yielding a rich and complex phenomenology.

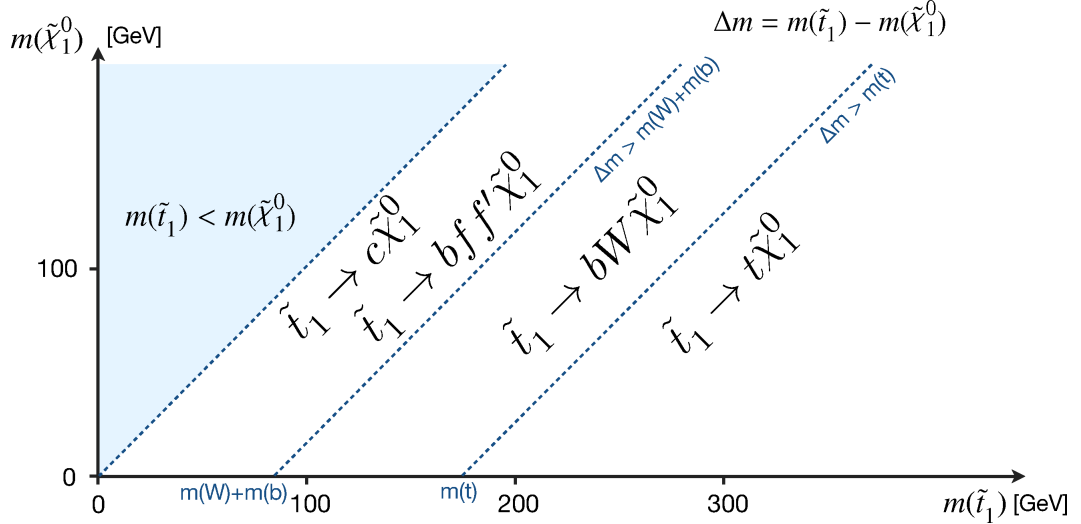


Figure 1.11: Stop decay modes in the  $m_{\tilde{t}}\text{-}m_{\tilde{\chi}_1^0}$  plane [38].

A favoured two-body decay of the  $\tilde{t}$ , shown Figure 1.12a, is the following:

$$\tilde{t}_1 \rightarrow t + \tilde{\chi}_1^0 \quad (1.36)$$

that requires  $m_{\tilde{t}_1} > m_t + m_{\tilde{\chi}_1^0}$ . In principle an analogous decay can happen into heavier neutralinos, yielding a more complex phenomenology, but this possibility is neglected in the present discussion. When a two-body decay takes place, the boost of the quarks and LSPs in the final state depends on the mass splitting  $\Delta m(\tilde{t}_1, \tilde{\chi}_1^0)$ . If the splitting is large the objects are produced with high momentum, while compressed mass spectra yield softer decay products, that often require dedicated analysis techniques. An alternative two-body decay, illustrated in Figure 1.12b, is:

$$\tilde{t}_1 \rightarrow b + \tilde{\chi}_1^+ \quad (1.37)$$

where the kinematic constraint is  $m_{\tilde{t}_1} > m_b + m_{\tilde{\chi}_1^+}$  and the mass of the  $\tilde{\chi}_1^+$  appears as a new free parameter. It should be noted that the decays in Figures 1.12a and 1.12b assume that the  $\tilde{t}$  decays exclusively in the channel of interest,  $t + \tilde{\chi}_1^0$  and  $b + \tilde{\chi}_1^+$  with 100% respectively. If both decays occur with comparable branching ratios (BRs) it is possible to obtain asymmetric final states as the one shown in Figure 1.12c, interesting to examine in addition to the symmetric ones.

Another possibility for a two-body final state [39] is:

$$\tilde{t}_1 \rightarrow c + \tilde{\chi}_1^i \quad (1.38)$$

but this decay is flavour-violating (FV) so it is expected to be relevant only when the competitive channels are kinematically forbidden, as in the compressed region in Figure

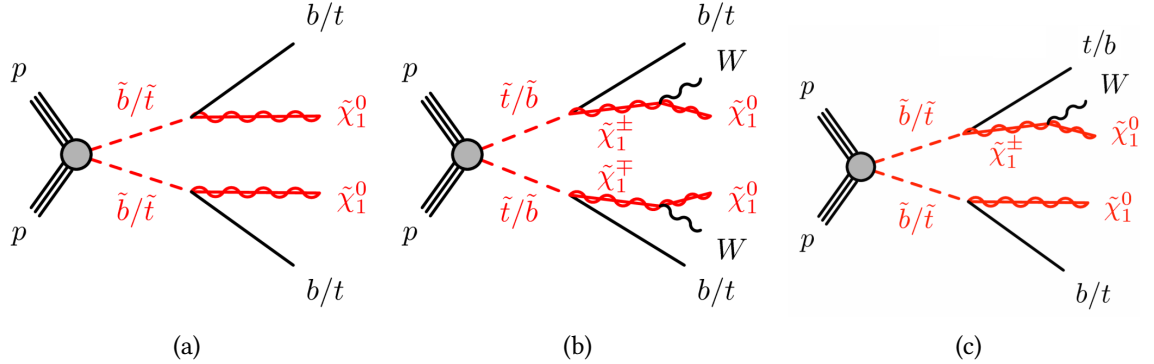


Figure 1.12: Stop quarks decaying directly into a  $\tilde{\chi}_1^0$  (a), via a  $b\tilde{\chi}_1^+$  (b) or into a mixture of the two final states (c). The figures show how the diagrams changes if  $\tilde{t}$  or  $\tilde{b}$  pair production is considered.

1.11.

As shown in Figure 1.12, the Feynman diagrams can easily be transformed from  $\tilde{t}$  to  $\tilde{b}$  pair-production by replacing the top quarks in the final state with bottom quarks. The replacement has an impact on the kinematic properties of the final state, because top quarks have a more complex experimental signature, so the analyses need to be adapted to the chosen case. A comprehensive search for  $\tilde{b}$  pair-production in various final states is discussed in detail in Chapter 5.

When two-body decays are kinematically forbidden, the off-shell decays of the  $\tilde{t}$  via virtual  $W$  bosons or top quarks become relevant, yielding three-body or four-body final states. The decay via a virtual top quark (Figure 1.13a) is:

$$\tilde{t}_1 \rightarrow b + W + \tilde{\chi}_1^0 \quad (1.39)$$

while the four-body decay where also the  $W$  is virtual gives:

$$\tilde{t}_1 \rightarrow b + f + f' + \tilde{\chi}_1^0 \quad (1.40)$$

As discussed in detail in Ref. [39], the four-body decay and the two-body decay into charm quarks (Equation 1.38) are in competition in the same region of the  $m_{\tilde{t}}\text{-}m_{\tilde{\chi}_1^0}$  plane, with a relative branching ratio that depends on the values of the MSSM parameters.

### *R*-parity violating decays

When the  $\tilde{t}$  decays via *R*-parity violating couplings, the assumption that the LSP must be a neutralino can be dropped and direct decays into Standard Model particles become

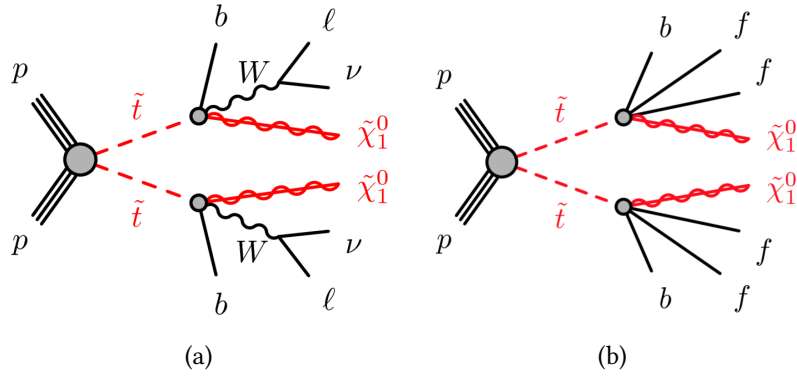


Figure 1.13: Three-body (a) and four-body (b) decays of the stop. For the three-body case, the leptonic decay of  $W$  bosons is shown.

possible. As discussed in Section 1.3.4, models with spontaneously broken  $U(1)_{B-L}$  symmetry predict the two-body decay of the  $\tilde{t}$  into a bottom quark and a lepton (see Equation 1.35) where the preferred lepton flavour is related to the neutrino mass hierarchy. This signal, shown in Figure 1.14a, yields two  $b\text{-}\ell$  pairs with invariant mass peaking at  $m_{\tilde{t}_1}$  and is targeted by the analysis presented in Chapter 6.

Finally, an alternative RPV coupling predicts the prompt decay of the  $\tilde{t}$  into a pair of quarks:

$$\tilde{t}_1 \rightarrow q + q' \quad (1.41)$$

The corresponding Feynman diagram is shown in Figure 1.14b, and the analysis is particularly challenging due to the overwhelming multijet background at the LHC.

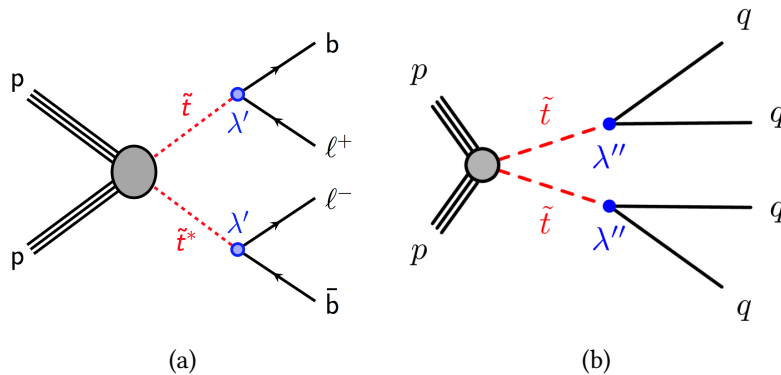


Figure 1.14: RPV decays of the stop into a  $b$ - $\ell$  pair (a) and two quarks (b).

# Chapter 2

## LHC and ATLAS

This thesis is centered on the analysis of proton-proton collisions delivered by the LHC accelerator [40] at CERN during the 2015 and 2016 operation at  $\sqrt{s} = 13$  TeV, and recorded by the ATLAS detector [41]. This chapter provides an overview of the experimental setup, starting from a discussion of the CERN accelerator complex (Section 2.1) and continuing with a description of ATLAS and its components (Section 2.3).

### 2.1 The LHC accelerator

The Large Hadron Collider (LHC) is a circular accelerator [42] located in a 27 km long underground tunnel at the European Organisation for Nuclear Research (CERN). It is able to accelerate two beams of protons in opposite direction, delivering collisions at a center of mass energy  $\sqrt{s} = 13$  TeV. The collisions take place in four interaction points, where particle physics detectors are employed to reveal and measure the fundamental physics processes that take place.

#### 2.1.1 Particle accelerators

The LHC is a circular machine with two beams travelling in opposite direction. The circular trajectory is maintained by an array of dipole magnets that produce a bending field orthogonal to the direction of motion of the particles. The relativistic relation

$$p = 0.3BR \quad (2.1)$$

expresses the momentum  $p$  of the particles (in GeV) as a function of the magnetic field  $B$  (in Tesla) and the radius  $R$  of the accelerator (in meters). The rate of physics collisions

delivered by the accelerator is measured by the instantaneous luminosity:

$$\mathcal{L}_{\text{inst}} \equiv \frac{1}{\sigma} \frac{dN}{dt} \quad (2.2)$$

where  $dN/dt$  is the rate of occurrence of a benchmark physics process and  $\sigma$  is its total cross section. The instantaneous luminosity is measured in inverse barn per second ( $b^{-1}s^{-1}$  where  $1 b \equiv 10^{-24} \text{ cm}^2$ ) and its value is independent of the particular process considered, so it can be expressed as a function of beam parameters:

$$\mathcal{L}_{\text{inst}} = f \frac{n_1 n_2}{4\pi\sigma_x\sigma_y}. \quad (2.3)$$

In the above expression  $f$  is the revolution frequency,  $n_1$  and  $n_2$  are the numbers of particles in the colliding bunches and  $4\pi\sigma_x\sigma_y$  is their transverse area at the interaction point, described by the gaussian widths  $\sigma_x$  and  $\sigma_y$ . The total amount of data delivered by the accelerator is given by the integrated luminosity:

$$\mathcal{L}_{\text{tot}} = \int_{t_1}^{t_2} \mathcal{L}_{\text{inst}} dt \quad (2.4)$$

with integral taken over the relevant period of operation. Circular colliders can operate at higher luminosity compared to linear accelerators, because the beams are kept in their trajectory for long periods of time, so the individual proton bunches can be repeatedly used for collisions instead of decelerating them after a single crossing.

The main limitation of circular colliders is the synchrotron radiation that charged particles emit when they experience transverse acceleration. The associated rate of energy loss is given by

$$\frac{dE}{dt} = \frac{E^4}{m^4 R} \quad (2.5)$$

where  $m$  is the mass of the accelerated particles and  $R$  is the radius of curvature of their trajectory. Since it is inversely proportional to  $m^4$ , the energy loss is extremely significant for light particles such as electrons or positrons, while for protons it is reduced by a factor  $(m_e/m_p)^4 \sim 10^{-12}$ . At electron-positron circular colliders, synchrotron radiation is the main effect that determines the maximum energy reach. Hadron colliders are less affected by this phenomenon, and the limiting factor for their energy is magnetic field of the bending magnets.

### 2.1.2 Physics at hadron colliders

At particle colliders with two beams of equal energy  $E$  the center of mass frame of the interactions corresponds to the laboratory frame, so the total energy of the collisions is

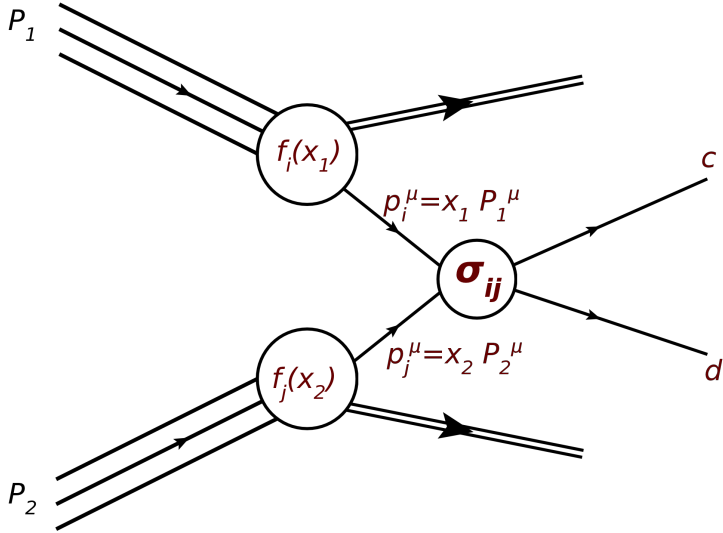


Figure 2.1: Hard scattering process involving two partons  $i$  and  $j$  whose momenta  $p_i$  and  $p_j$  are a fraction  $x_1$  and  $x_2$  of the total momenta of the protons. [45]

simply given by  $\sqrt{s} = 2E$ . This general statement, however, is only partially valid at hadron colliders, where the physics processes of interest are produced by the scattering of individual partons (quarks or gluons) that carry an unknown fraction  $x_1$  and  $x_2$  of the momentum of the hadron [43]. A scheme of a hard scattering process at a hadron collider is given in Figure 2.1, where all the main elements are highlighted. In each collision, the partonic center of mass energy  $\sqrt{\hat{s}}$  is smaller than  $\sqrt{s}$  and can be expressed as:

$$\sqrt{\hat{s}} = x_1 x_2 \sqrt{s}, \quad (2.6)$$

where  $x_1$  and  $x_2$  vary on an event-by-event basis following probability density functions  $f_i(x_1, Q^2)$  and  $f_j(x_2, Q^2)$ . These distributions are known as parton distribution functions (PDFs) and measured by a fit to collision data from experimental observables in various processes and at different energy scales [44]. The total cross section of a generic physics process  $ij \rightarrow X$  can be expressed as:

$$\sigma_{ij} = \int dx_1 dx_2 f_i(x_1, Q^2) f_j(x_2, Q^2) \hat{\sigma}_{ij \rightarrow X}, \quad (2.7)$$

where the contribution of the PDFs and the partonic cross section  $\hat{\sigma}$  are factorised. It should be noted that, since  $x_1$  and  $x_2$  can have different values, the physics objects  $X$  produced by the hard interaction carry an unknown boost in the direction of the beam axis. In addition, the final state contains extra objects produced by the partons that are not involved in the hard scattering, characterised by low transverse momentum and small production angles with respect to the beam. These underlying objects are a major

source of background at hadron colliders.

Underlying hadronic activity in the events can also be generated by proton-proton collisions where no hard scattering takes place. From a comparison between the total cross sections of inelastic collisions and of any other Standard Model process (Figure 1.10) it follows that the majority of the interactions yield only soft hadronic objects in the final state, while the hard scattering happens only occasionally. For every crossing between proton bunches, it is possible to compute the average number of interactions  $\langle \mu \rangle$ , commonly referred to as pileup, as a function of the instantaneous luminosity, the number of circulating bunches  $n_b$ , their frequency  $f$  and the total cross section of inelastic scattering of the protons  $\sigma_{\text{inel}}$ :

$$\langle \mu \rangle = \frac{\sigma_{\text{inel}} \mathcal{L}_{\text{inst}}}{n_b f}. \quad (2.8)$$

As described in Section 2.1.4, the amount of pileup at the LHC is significant and its effects need to be kept under control when performing physics analyses.

### 2.1.3 The purpose of the LHC

The construction of the Large Hadron Collider (LHC) at CERN was approved in December 1994 to replace the existing electron-positron accelerator, the LEP [46]. At the time, the largest machines in operation were the Tevatron [47], a proton-antiproton collider located at the Fermilab National Laboratory in the US, and the LEP itself, whose 27 km underground tunnel is now used for the LHC. The LEP experiments were able to provide precise measurements of electroweak processes [48], thanks to the large number of  $Z$  and  $W$  bosons produced by the electron-positron collisions with low background rates. In parallel, the top quark was discovered at the Tevatron [49, 50] using proton-antiproton beams at a collision energy of 1.8 TeV (subsequently increased to 1.96 TeV). Despite their major results, however, neither the LEP [51] nor the Tevatron [52, 53] were able to detect the Higgs boson, whose discovery was essential to demonstrate the validity of the spontaneous symmetry breaking mechanism in the Standard Model. Due to the relevance of the issue, a final statement on its existence had to be a primary goal of any new experiment in construction.

The purpose of the new accelerator was to produce collisions at an unprecedented center of mass energy, larger by one order of magnitude with respect to the Tevatron and by two orders of magnitude with respect to the LEP. To achieve this goal, the only possible option was to build a hadron collider, because electron-photon machines are limited by the emission of synchrotron radiation (Equation 2.5). The ultimate goal, in addition to the detection of the elusive Higgs boson, was the exploration of the energy frontier, in

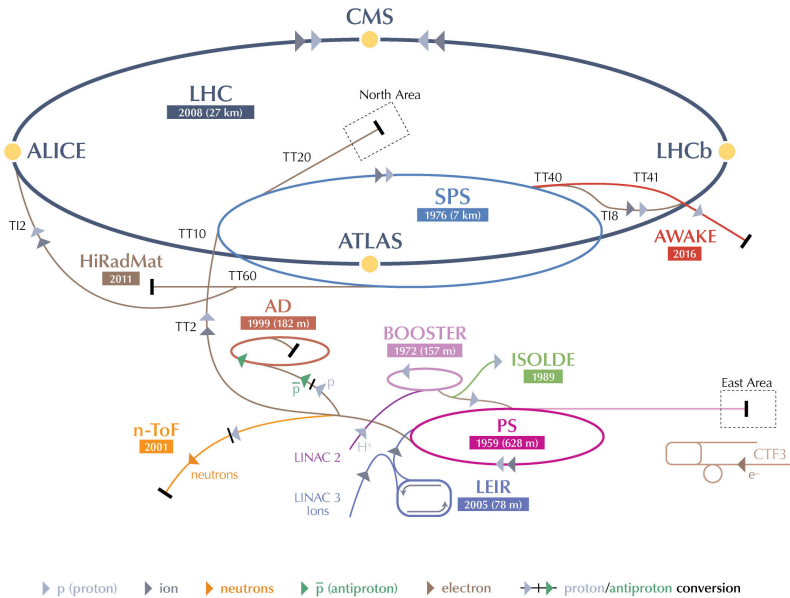


Figure 2.2: Scheme of the experimental facilities of CERN, showing the accelerator complex and the associated experiments.

order to provide answers to the many open problems of the Standard Model presented in Section 1.2.

The LHC was designed with two beams of protons, contrarily to what was done for the Tevatron where one of the two beams was made of antiprotons. In general, the advantage of colliding protons with antiprotons is that the cross section of processes mediated by quark-antiquark annihilation increases, because the antiquark content of antiprotons is higher. However, at the characteristic center of mass energy of the LHC the main production channels of the most relevant processes are mediated by gluons, which are equally present in protons and antiprotons. Since antiproton beams with high intensity are difficult to produce, it was chosen to run the machine with proton beams to maximise the instantaneous luminosity.

Finally, the LHC was also designed to deliver collisions of lead ions, for a dedicated physics programme aimed at studying the thermodynamical properties of QCD and the quark-gluon plasma. This programme is beyond the scope of this thesis, so the operation with lead ions is not further described.

	Design	2015	2016
$\sqrt{s}$ [TeV]	14	13	13
Maximum $n_b$	2808	2244	2220
Average $\langle \mu \rangle$	-	13.7	24.9
Maximum $\langle \mu \rangle$	19	28.1	52.2
Peak $\mathcal{L}_{\text{inst}}$ [ $10^{33} \text{cm}^{-2}\text{s}^{-1}$ ]	10	5.0	13.8
$\mathcal{L}_{\text{tot}}$ for physics [ $\text{fb}^{-1}$ ]	-	3.2	32.8

Table 2.1: Performance parameters of the LHC during the 2015 and 2016 operation as measured by the ATLAS experiment [55], compared to the design values from Ref. [42].

### 2.1.4 The CERN accelerator complex and the LHC

Figure 2.2 shows the full infrastructure of the CERN laboratory that prepares the proton beams for the injection in the LHC at an energy of 450 GeV [54]. Protons are produced through the ionisation of a hydrogen source, then they are accelerated to 50 MeV by a linear accelerator called LINAC 2. They are then injected in the first circular machine, the Proton Synchrotron Booster (PSB), that increases their energy up to 1.4 GeV and prepares them for the following step, the Proton Synchrotron (PS). The PS is the oldest accelerator of CERN still in operation: it was built in 1959 and today it is used to accelerate the protons from 1.4 to 26 GeV. The next stage is the Super Proton Synchrotron (SPS), where the  $W$  bosons were discovered in 1983 by the UA1 and UA2 collaborations. The SPS is now used to increase the energy of the protons up to 450 GeV, so that they can finally be injected in the LHC.

#### The LHC operation

The design report [42] published in 2004 describes the expected performance of the LHC before its construction, as summarised in Table 2.1 in comparison with the 2015 and 2016 runs. The center of mass energy is designed to be  $\sqrt{s} = 14$  TeV with a maximum instantaneous luminosity of  $\mathcal{L}_{\text{inst}} = 10^{34} \text{cm}^{-2}\text{s}^{-1}$ , to be obtained with a beam split into 2808 bunches of  $\sim 10^{11}$  protons each. During the first years of operation the performance of the LHC has generally met the expectations, with the majority of the parameters matching the targets or even exceeding them.

The first run of the LHC (Run 1) began when the first beams circulated in the machine on September 10<sup>th</sup>, 2008. After 9 days of operation a serious incident was caused by

the excessive heating of a superconductive cable in the connection between two magnets, seriously damaging a whole sector of the accelerator. After a necessary shutdown period of one year, the first proton collisions took place in fall 2009 at the minimum center of mass energy  $\sqrt{s} = 900$  GeV. In 2010 and 2011 the LHC delivered two extended periods of data taking at  $\sqrt{s} = 7$  TeV reaching  $\mathcal{L}_{\text{inst}} = 2 \times 10^{32} \text{cm}^{-2}\text{s}^{-1}$  and  $\mathcal{L}_{\text{inst}} = 3.65 \times 10^{33} \text{cm}^{-2}\text{s}^{-1}$  respectively. In 2012 the energy of the collisions was raised to  $\sqrt{s} = 8$  TeV, reaching a maximum  $\mathcal{L}_{\text{inst}} = 8 \times 10^{33} \text{cm}^{-2}\text{s}^{-1}$  and accumulating a total integrated luminosity  $\mathcal{L}_{\text{tot}} = 20 \text{fb}^{-1}$ . At the end of Run 1 the LHC had almost reached the design value of the instantaneous luminosity, while the center of mass energy was still significantly below the target due to the problems with the superconducting cables in the magnets.

After a long shutdown period of two years, the second run of the LHC (Run 2) began in spring 2015 at  $\sqrt{s} = 13$  TeV, close to the design value of the center of mass energy. Table 2.1 shows how the machine performed during the first two years of Run 2, during which the data analysed in this thesis were collected. The cumulative integrated luminosity versus time recorded by the ATLAS experiment is presented in Figures 2.3a and 2.3b for 2015 and 2016 respectively. Figure 2.4a shows the distribution of the average number of interactions per bunch crossing  $\langle\mu\rangle$  (see Equation 2.8) during the 2015 and 2016 runs: the increase in instantaneous luminosity in 2016 caused a larger amount of pileup in the experiments. Finally, in Figure 2.4b the peak luminosity is plotted for every fill of the 2016 run, during which the performance of the LHC has significantly exceeded the design targets.

At the time of writing Run 2 is still ongoing. In 2017 the LHC delivered an additional dataset comparable to the one of 2016, reaching new record values of instantaneous luminosity and  $\langle\mu\rangle$  at  $\sqrt{s} = 13$  TeV. Another year of data taking is scheduled for 2018, after which a second long shutdown will begin. Since the analyses presented in this thesis are only using the data from the 2015 and 2016 runs, the more recent datasets are not further discussed.

## 2.2 The LHC experiments

The LHC serves seven different experiments, all located along its ring. The main experiments, ATLAS [41], CMS [56], LHCb [57] and Alice [58], are built in correspondence with the four interaction points where the collisions take place, as indicated by the yellow circles in figure 2.2. In addition there are three smaller experiments, TOTEM [59], LHCf [60] and MoEDAL [61]. A short description of their main purpose is provided

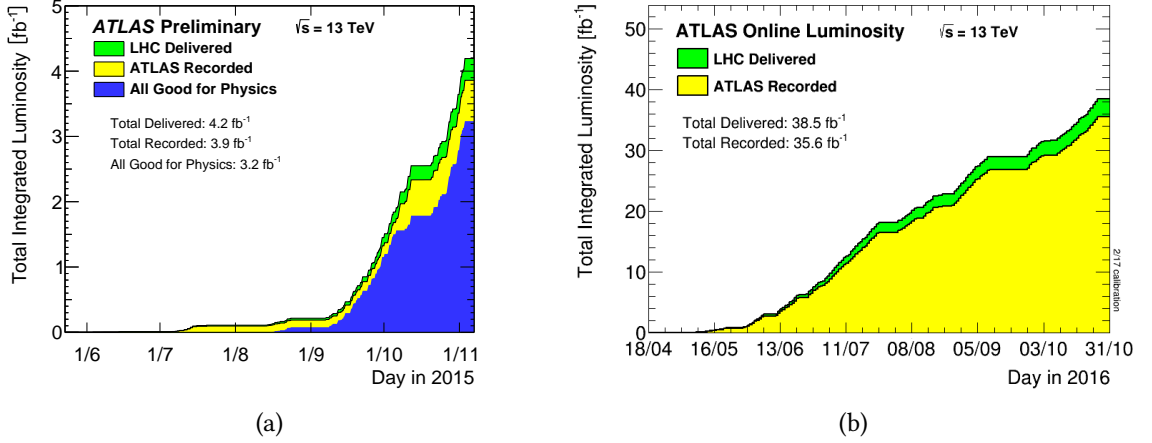


Figure 2.3: Total integrated luminosity delivered by the LHC and recorded by the ATLAS detector in 2015 (a) and 2016 (b). For 2015 the figure includes the histogram obtained after further quality criteria are applied to the data to make them available for physics analyses. The majority of the dataset analysed in this thesis are part of the 2016 dataset.

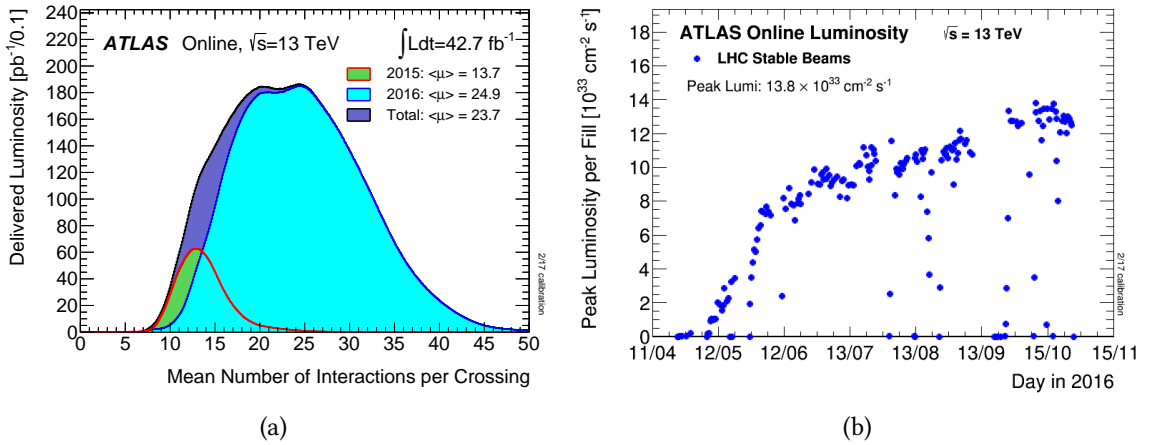


Figure 2.4: Distribution of the average number of interactions per bunch crossing  $\langle \mu \rangle$  (see Equation 2.8) during the 2015 and 2016 runs (a) and maximum instantaneous luminosity for every fill in the 2016 run (b) as measured by the ATLAS detector.

below:

**ATLAS and CMS** are the two largest detectors at the LHC. They are both general-purpose experiments, designed with different technologies to search for the Higgs boson and to explore the energy frontier at the TeV scale.

**LHCb** is a forward detector optimised to the study the decays of  $B$  and  $D$  mesons in proton-proton collisions, providing precision tests of the Standard Model parameters with special attention to CP violation.

**ALICE** is an asymmetric detector optimised for lead ion collisions. Its purpose is to study the properties of QCD phase transitions and quark gluon plasma.

**TOTEM** is a smaller experiment mounted next to the CMS detector along the LHC tunnel. It is used to monitor the LHC luminosity by providing measurements of the total, elastic and diffractive cross-section of proton-proton collisions in the forward region, at small angles with respect to the beam.

**LHCf** is a second forward detector located at both sides of the ATLAS cavern. Its purpose is to simulate cosmic ray shower processes by using particles scattered at small angles with respect to the beam axis.

**MoEDAL** is mounted next to the LHCb detector and is used to search for direct evidence of magnetic monopoles or highly ionising Stable Massive Particles (SMPs).

### 2.2.1 General-purpose experiments

As anticipated, the main purpose of ATLAS and CMS is to investigate the existence of new particles at heavy mass scales, with particular attention to the Higgs boson. Since the experimental signature of new physics beyond the Standard Model is unknown, both detectors are designed to identify as many different types of objects as possible, in order to maximise the chances of a discovery.

An essential feature of general-purpose detectors is hermeticity. Hermetic detectors (also known as  $4\pi$  detectors) are designed to observe all possible products of the collisions by covering the largest possible area around the interaction region. They are split in multiple sub-systems that provide the necessary information to identify and distinguish the different types of particles, with fine granularity in order to determine their position. If all particles with non-negligible interaction properties are measured with sufficient precision, hermetic detectors can reveal the presence of invisible objects such as neutrinos

or dark matter by reconstructing the resulting momentum imbalance in the transverse plane ( $E_T^{\text{miss}}$ ).

The detectors must also satisfy general requirements common to all experiments at the LHC. The accelerator provides a collision rate of 40 MHz, setting the scale of the speed of response that each detector component must have to discriminate between subsequent events. A complex trigger and data acquisition system is needed to select the events where interesting physics objects are produced, saving the relevant information to permanent storage for offline analysis. Another important feature is resistance to radiation, especially for the detector components located at small distance from the interaction region.

ATLAS and CMS implement the above requirements using different technologies, in order to provide independent measurements of the same physics phenomena. Their overall performance is similar and the agreement between their results is a fundamental test of their reliability.

## 2.3 The ATLAS detector

ATLAS (A Toroidal Lhc ApparatuS) is the largest detector at the LHC. The full system weights approximately 7 kTons and has a cylindrical symmetry centered around the beam axis, with a transverse diameter of 25 m and a longitudinal length of 44 m. The original design of the detector was proposed in 1994 [62], then its components were developed and assembled in parallel with the construction of the LHC accelerator. The first data were taken in 2008 with cosmic rays and the first proton collisions were recorded in 2009 at  $\sqrt{s} = 900$  GeV.

A schematic view of the detector is provided in Figure 2.5, where the main subsystems are highlighted. The apparatus is designed to meet the requirements of a general-purpose experiment, with special attention to the products of hard scattering with large transverse momentum ( $p_T$ ) with respect to the beam axis. The detector consists of a set of concentric layers surrounding the interaction region, and can be divided into four major components. The Inner Detector (see Section 2.3.3) reconstructs the ionisation tracks of charged particles and can be used to identify their production and decay vertices. Two calorimeters (Section 2.3.4) are then employed to measure the energy of electromagnetic and hadronic objects, while a Muon Spectrometer (Section 2.3.5) is placed in the outermost layer to identify muons that travel through the detector. A magnet system (Section 2.3.2) is employed to bend the trajectories of charged particles in the Inner Detector and Muon Spectrometer, allowing the measurement of their momenta. In order to maximise

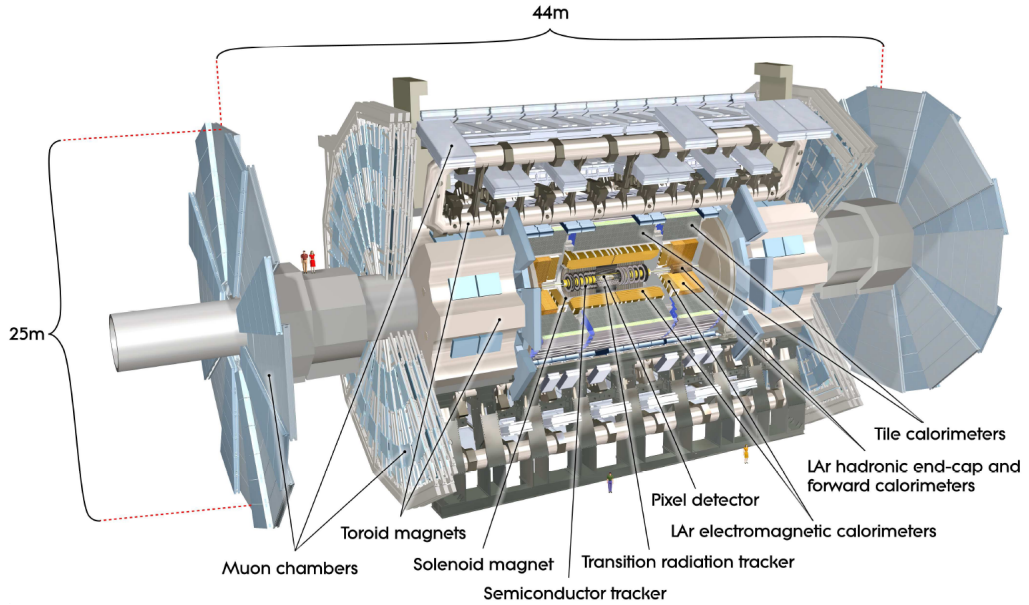


Figure 2.5: Overview of the ATLAS detector and its components.

the hermeticity of the detector, each sub-system is made of components that are parallel to the beam axis (barrels) and orthogonal to it (end-caps).

### 2.3.1 Coordinate system and event display

In ATLAS the direction of the beam defines the  $z$  axis of a cartesian reference frame, with origin located at the center of the interaction region. The transverse section of the detector is mapped by the  $x$  and  $y$  coordinates, with the  $x$  axis pointing towards the center of the LHC ring. Due to the symmetry of the system, it is natural to introduce cylindrical coordinates replacing  $x$  and  $y$  with the polar angle  $\theta$  and the azimuthal angle  $\phi$ . The polar angle is commonly translated into the pseudorapidity  $\eta$ , defined as

$$\eta = -\log \left[ \tan \left( \frac{\theta}{2} \right) \right]. \quad (2.9)$$

In the limit of massless objects  $\eta$  is additive with respect to boosts in the  $z$  direction, so any difference in pseudorapidity is a Lorentz invariant. This feature is particularly useful at a hadron collider such as the LHC, where the particles are produced with an unknown longitudinal boost due to the variable fraction of momentum carried by the partons (see Section 2.1.2).

Figure 2.6 shows a scheme of the transverse section of the ATLAS detector, illustrating the characteristic signatures of the main types of particles:

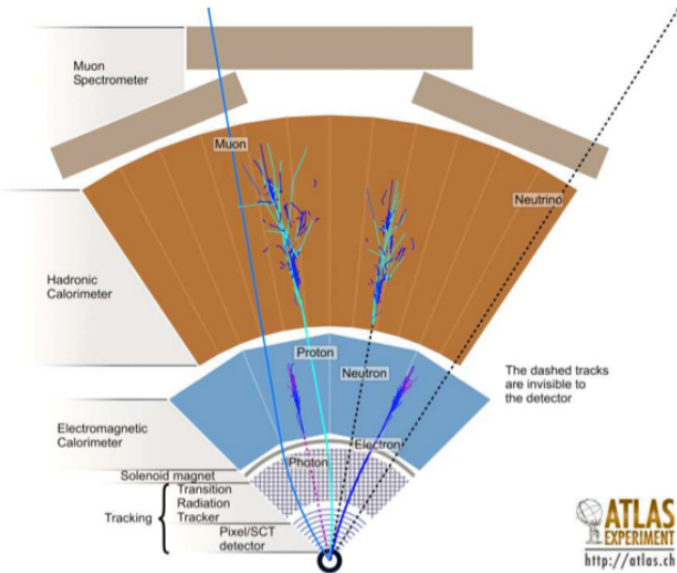


Figure 2.6: Transverse section of the ATLAS detector, showing the characteristic signatures of the main types of particles.

**Photons** are neutral objects, so they appear as showers in the electromagnetic calorimeter with no associated ionisation track in the Inner Detector.

**Electrons** are identical to photons in the calorimeter, but they also produce a track in the Inner Detector.

**Neutrons** generate a shower in the hadronic calorimeter and no tracks in the Inner Detector.

**Protons** add an Inner Detector track to the characteristic signature of neutral hadrons.

**Muons** travel through each layer of the detector yielding ionisation tracks in the Inner Detector and in the Muon Spectrometer.

**Neutrinos** leave no signal in the detector, so their presence can only be inferred by reconstructing momentum imbalance in the transverse plane.

### 2.3.2 Magnet system

The ATLAS magnet system [63], shown in Figure 2.7, provides the bending field that curves the trajectories of charged particles in the Inner Detector and in the Muon Spectrometer. The magnets are split in two components: a solenoid, located around the Inner

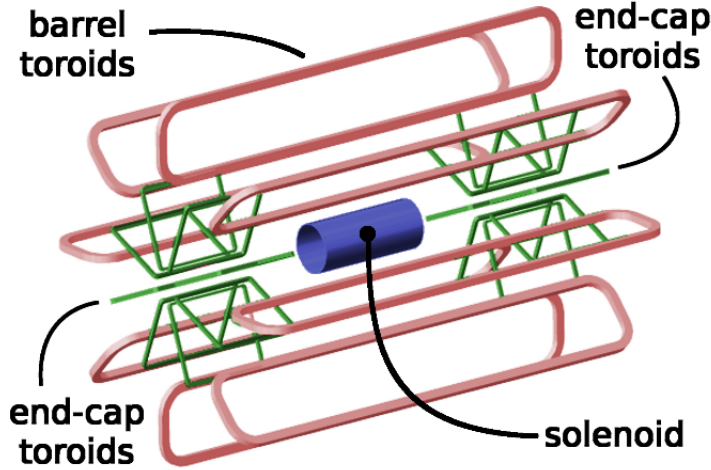


Figure 2.7: ATLAS magnet system.

Detector, and an outer system consisting in a set of barrel and end-cap toroids, that provide the magnetic field to the Muon Spectrometer. The layout of the magnet system distinguishes ATLAS from CMS, where a single solenoid magnet is employed [64], and has driven the design of the remaining parts of the detector.

**Solenoid** The solenoid magnet surrounds the Inner Detector described in Section 2.3.3, providing a magnetic field of 2 T using a nominal current of 7.73 kA that runs through 9 km of superconducting NbTi wires. The total length of the solenoid is 5.8 m, while the internal radius is 1.2 m and the thickness is only 4.5 cm, in order to minimise the amount of material placed in front of the calorimeters.

**Toroids** The barrel and end-cap toroids of ATLAS are both made of 8 identical magnets, that surround the calorimeter system with an azimuthal symmetry around the axis of the detector. The barrel system is 25.3 m long and has an outer diameter of 20.1 m, while the end-caps have a length of 5.3 m and 10.7 m of diameter. The peak field produced by both barrel and end-cap toroids is 4 T, obtained with a nominal current of 20.5 kA.

### 2.3.3 Inner Detector

The Inner Detector (ID) [65] is located at the core of the ATLAS experiment, immediately around the interaction region where the collisions take place. Its purpose is to reconstruct the tracks of charged particles in the events, with a pseudorapidity coverage  $|\eta| < 2.5$ . As shown in Figure 2.8, the system is organised in cylindrical layers where the

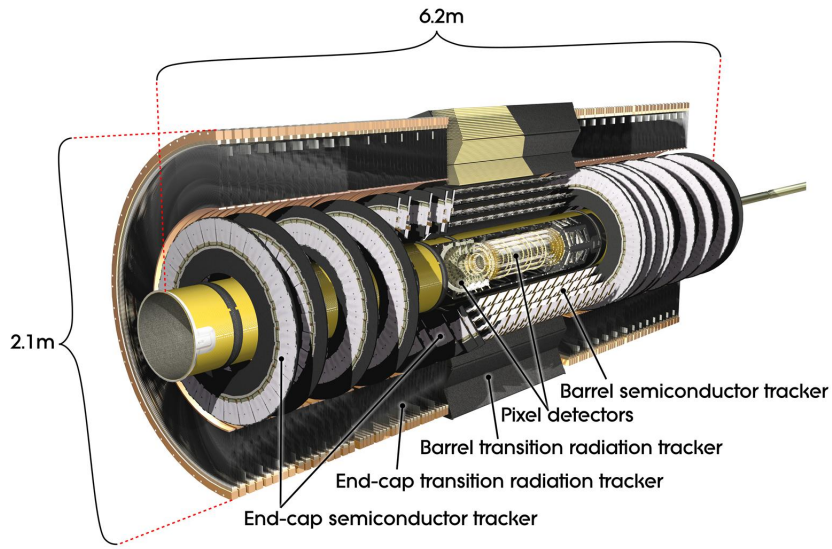


Figure 2.8: Transverse view of the barrel components of the ATLAS Inner Detector.

particles interact and release a localised signal. Due to the large multiplicity of particles produced by proton collisions, each layer needs to be finely segmented in order to provide an accurate measurements of the position of the hits, with enough precision to distinguish the individual tracks. Since the system is placed in proximity of the beam, it is also important to ensure that the hardware components are able to resist the high dose of radiation that they receive during the operation. Finally, the amount of material in the ID needs to be small in order to minimise the particle interactions before the calorimeter, that degrade the quality of the energy measurement.

The ID is split in three different subdetectors: a silicon Pixel detector, that includes an Insertable B-Layer (IBL) installed before the beginning of Run 2 in 2015, a Semi-Conductor Tracker (SCT) and a Transition Radiation Tracker (TRT). Each of them has a cylindrical symmetry, with the usual barrel and end-cap structure. Overall, the Inner Detector measures 6.2 m in length and 2.1 m in diameter.

### Pixel detector

The Pixel detector [66] is the innermost part of the ID, designed to provide tracking information with the finest level of granularity. As shown in Figure 2.9, the barrel part is made of four cylindrical layers of modules: the IBL [67, 68] (at 33.25 mm of distance from the beam axis), the b-layer or L0 (50.5 mm), the L1 (88.5 mm) and the L2 (122.5 mm). The end-caps consist of three circular disks, that contribute to achieve the desired longitudinal acceptance  $|\eta| < 2.5$ . The silicon pixels have a different segmentation in

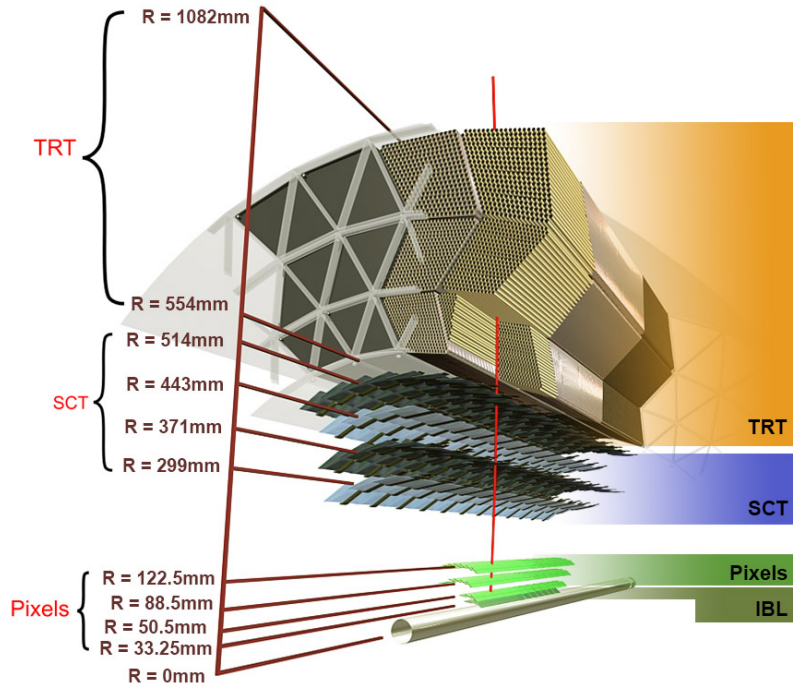


Figure 2.9: Transverse view of the ATLAS Inner Detector, showing the different layers.

the  $R\text{-}\phi$  and  $z$  directions: the smallest size in the  $R\text{-}\phi$  plane is  $50 \mu\text{m}$ , while the minimum longitudinal size is  $250 \mu\text{m}$  in the IBL and  $400 \mu\text{m}$  in the other layers. Due to the cost of the technology, it was chosen to use the Pixels only in the innermost layers of the ID, where it is essential to maximise the spacial resolution.

### Semi-Conductor Tracker

The SCT [69,70] is the intermediate part of the ID, consisting of four barrel layers and two end-caps with nine disks each. The components of the SCT are made of silicon, but the pixels are replaced by strips of  $80 \mu\text{m} \times 12 \text{ cm}$  to cover a larger area of space compared to the innermost layers. The strips are parallel to the direction of the beam in the barrels, while they are disposed radially in the end-caps. The individual layers are made of a pair of strip sensors, arranged at a relative angle of  $40 \text{ mrad}$ . This geometrical solution allows to obtain a good measurement of the position of the hits in the longitudinal direction, despite the significant length of the strips. The SCT is able to provide a spacial resolution of  $16 \mu\text{m}$  in the  $R\text{-}\phi$  plane and of  $580 \mu\text{m}$  in the  $z$  direction.

### Transition Radiation Tracker

The TRT [71,72] occupies the external layer of the ID, with radius between  $55.4 \text{ cm}$  and

108.2 cm. Unlike the inner layers, this system is based on the use of straw detectors with 4 mm of diameter and maximum length of 144 cm, filled with a mixture of Xenon (70%), CO<sub>2</sub> (27%) and Oxygen (3%). Similarly to the SCT strips, the straw tubes are located in a barrel, where they are parallel to the beam direction, and in two end-caps, where they are arranged radially. Each straw is crossed by a thin tungsten wire that serves as anode, so the device operates as a small drift chamber that measures the ionisation produced by the charge particles that cross it. A crucial feature of the TRT is that the region between the tubes is occupied by radiating material, where the particles emit x-rays proportionally to their relativistic  $\gamma$  factor. These photons are known as transition radiation, because they are generated when the particles cross the boundary between two media with different dielectric constants. The transition radiation is absorbed by the Xenon atoms in the tubes, and it is significantly larger for electrons than for heavier objects, because their average  $\gamma$  factor is greater. As a result, the TRT is able to provide a useful measurement to discriminate between electrons and other types of particles. Thanks to its geometry, the TRT yields a large number of hits ( $\sim 30$ ) for each track in the  $R\text{-}\phi$  direction, with longitudinal acceptance  $|\eta| < 2$  and a spacial resolution of 130  $\mu\text{m}$ .

### 2.3.4 Calorimeter system

The calorimeter system of ATLAS surrounds the the Inner Detector and the solenoid magnet and provides a measurement of the energy of electrons, photons and hadrons, that generate showers of particles as a result of their interaction with the materials. The characteristic parameters describing the depth of electromagnetic and hadronic showers are the radiation length  $X_0$  and the interaction length  $\lambda_I$ , with  $\lambda_I \gg X_0$  for all common materials. The detectors are designed to provide a full containment of the showers, and they are segmented in cells in order to obtain localised measurements of the energy deposits.

As shown in Figure 2.6, ATLAS employs two different types of calorimeters: the inner component is the Electromagnetic Calorimeter (ECAL) dedicated to electrons and photons, while the outer part is the Hadronic Calorimeter (HCAL) optimised for strongly interacting particles. The ECAL and HCAL are based on a sampling technology, in which the material that absorbs the incoming particles is distinct from the one that measures their energy. In addition, both calorimeters are non-compensating, which means that they have a different signal response to electrons and hadrons, so a dedicated scale factor must be applied to calibrate the two components of the showers at the same energy scale. In order to increase the longitudinal acceptance of the detector, two Forward

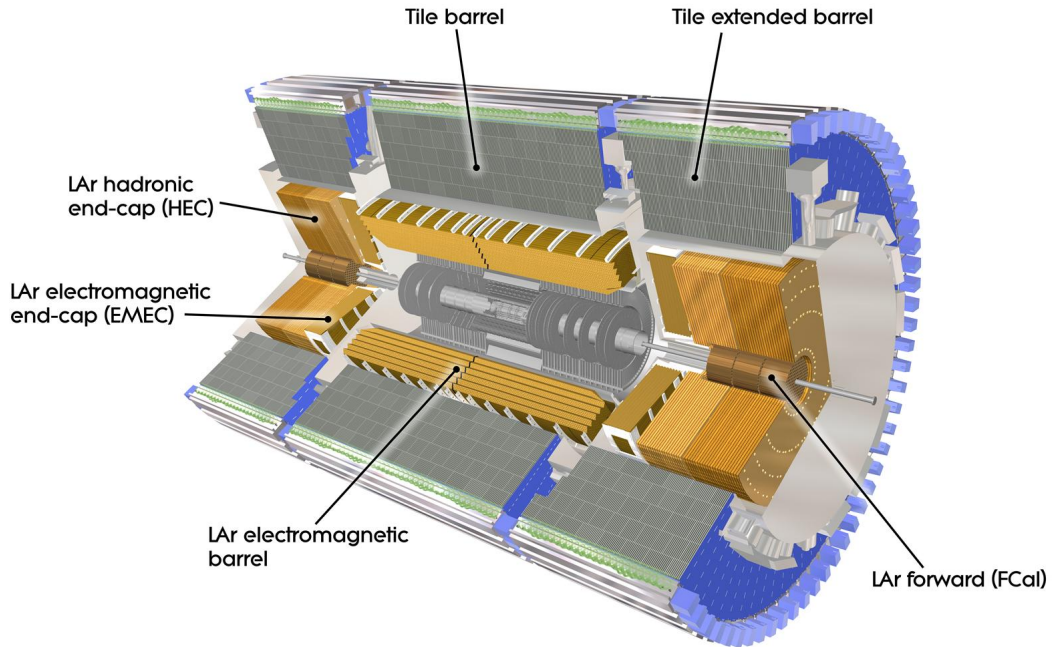


Figure 2.10: Section of the calorimeter system of the ATLAS, highlighting the different components of the ECAL and the HCAL.

Calorimeters (FCAL) are mounted on the opposite end-caps close to the beam pipe.

### Electromagnetic calorimeter

The ECAL [73] is a sampling calorimeter that employs lead (Pb) plates as absorbers and liquid argon (LAr) ionisation chambers with copper electrodes as active components. The system is divided into a central barrel, with an acceptance  $|\eta| < 1.475$ , and two end-caps with range  $1.375 < |\eta| < 3.2$ . The lead plates are arranged radially with a characteristic accordion geometry, that provides a full azimuthal coverage and avoids the presence of cracks in the  $\phi$  direction. The choice of LAr is motivated by its linear response combined with large signal yields and good resistance to radiation damage, while a limiting factor comes from its poor time resolution (400 ns), longer than the distance between two subsequent events.

The ECAL is finely segmented in cells in the  $\eta\text{-}\phi$  direction and it is composed of three layers, each with specific properties and purposes. The first layer has a thickness of  $4.3 X_0$  and a fine granularity in the  $\eta\text{-}\phi$  plane, which is needed to obtain a precise measurement of the initial development of the showers. Thanks to its segmentation, this layer

plays a key role in the discrimination between showers produced by single photons and showers that originate from the decay of neutral pions ( $\pi_0$ ) into two photons. The second layer measures  $16 X_0$  in thickness, and provides additional information which is used to determine the position and direction of the showers. The third layer has a depth of  $2 X_0$  and is used to measure the leakage of electromagnetic showers beyond the ECAL, contributing to the discrimination between electromagnetic and hadronic showers. The ECAL is completed by a presampler layer of LAr with no passive material, which is placed in the solenoid magnet in order to measure the particle interactions in the inner parts of the detector.

In total, the ECAL has a thickness of  $22 X_0$  in the barrel for particles with  $\eta = 0$ , which grows as a function of pseudorapidity reaching  $33 X_0$  in the barrel and up to  $38 X_0$  in the end-caps. The longitudinal segmentation of the components of the ECAL produces a few crack regions where the nominal performance is deteriorated. This happens at  $\eta = 0$  due to a 4 mm gap in the central barrel, at  $1.37 < |\eta| < 1.52$  due to the transition between barrel and end-caps, and at  $|\eta| = 2.5$  where there is a small gap between two end-cap crowns.

### **Hadronic calorimeter**

The HCAL is dedicated to the measurement of the hadronic showers, that are only partially contained by the ECAL. As shown in Figure 2.10, the full system consists of a barrel, two extended barrels and two Hadronic End-Caps (HEC).

The barrel and extended barrels form the Tile Calorimeter (TileCal) [74], which uses steel tiles as absorbers and plastic scintillators as active material. The barrel covers the central pseudorapidity region  $|\eta| < 1.0$ , while the extended barrels have a range  $0.8 < |\eta| < 1.7$ , with a partial overlap aimed at reducing the impact of the cracks. Similarly to the ECAL barrels, both central and extended barrels of TileCal are divided into three layers, with an approximate thickness of 1.5, 4.1 and 1.8 interaction lengths in the central component and of 1.5, 2.6 and 3.3 interaction lengths in the extended ones. Finally, the HEC is composed of two independent end-caps made of LAr and copper (Cu), that increase the pseudorapidity coverage of the detector to  $1.5 < |\eta| < 3.2$ .

Figure 2.11 from Ref. [41] shows the cumulative amount of material, in units of interaction length  $\lambda_I$ , as a function of the pseudorapidity  $\eta$  in the various layers of the detector. The total thickness is at least  $10 \lambda_I$  in all pseudorapidity regions, with peaks and dips caused by the transition between different components.

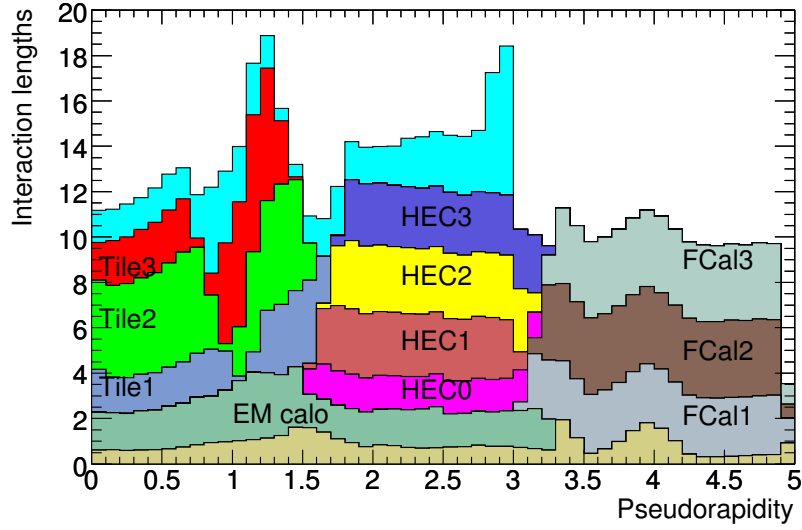


Figure 2.11: Total occupancy of the major components of the detector in units of interaction length, as a function of the pseudorapidity  $|\eta|$ . The graph shows the material in front of the ECAL, the different layers of ECAL and HCAL including the forward components, and also the total amount of material in front of the first active layer of the muon spectrometer up to  $|\eta| < 3.0$ .

### Forward calorimeter

The calorimeter system is completed by a forward detector (FCal) that provides electromagnetic and hadronic energy measurements in the pseudorapidity range  $3.1 < |\eta| < 4.9$ . The FCal uses LAr as active material and is divided in three layers of 45 cm each. The inner layer uses copper as absorber and is dedicated to electromagnetic showers, while the remaining two are made of tungsten and are optimised to measure the hadronic ones. The measurements performed by the FCal are not as accurate as those from the other subdetectors, due to a coarser segmentation and to the large amount of background from underlying hadronic activity in the forward region. Nevertheless, they give an crucial contribution to the hermeticity of ATLAS, which is important for the measurement of the momentum imbalance in the transverse plane ( $E_T^{\text{miss}}$ ).

### 2.3.5 Muon Spectrometer

The outermost component of ATLAS is the Muon Spectrometer (MS) [75] dedicated to the detection of muons, that travel through the inner layers of the detector as minimum ionising particles. The muon trajectory in the MS is curved in the  $R$ - $z$  plane by the

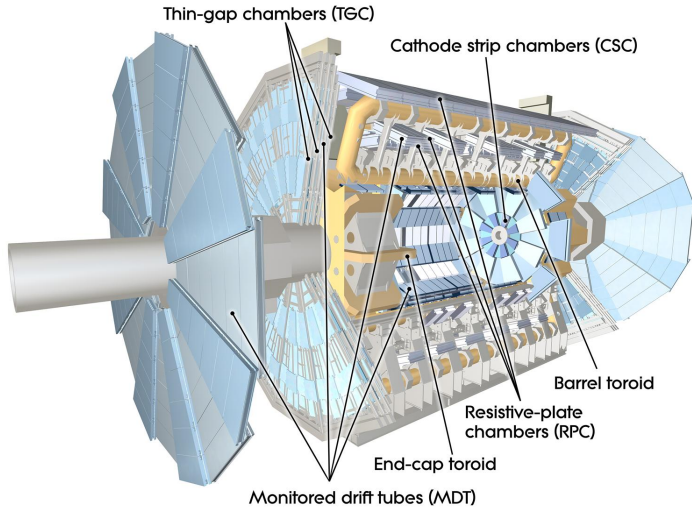


Figure 2.12: Scheme of the ATLAS outer layer showing the Muon Spectrometer.

bending field of the toroid magnets, so the reconstruction of the tracks can be used for the measurement the momentum, similarly to what happens in the Inner Detector. The larger size of the MS allows to provide accurate measurements of muons up to the TeV scale, which is essential for the physics program of ATLAS.

The MS consists a central barrel with three cylindrical layers with a radius of 5, 7.5 and 10 m, and four end-cap wheels at a longitudinal distance of 7.4, 10.8, 14 and 21.5 m from the center of the detector. This structure hosts four different subsystems shown in Figure 2.12, each contributing to specific needs of the detector. Monitored Drift Tube (MDT) chambers and Cathode Strip Chambers (CSC) are dedicated to high-resolution measurements of the tracks in the pseudorapidity range  $|\eta| < 2.7$ , while Resistive Plate Chambers (RPC) and Thin Gap Chambers (TGC) are designed to provide trigger information with faster speed of response. A brief description of the four components of the MS is given below.

**Monitored Drift Tubes** The MDTs are chambers composed of drift tubes with 30 mm of diameter, filled with a mixture of Argon and CO<sub>2</sub>. They cover the pseudorapidity range  $|\eta| < 2.7$ , except in the innermost end-cap layer where they only reach  $|\eta| < 2.0$ , providing a spatial resolution of approximately 80  $\mu\text{m}$  per tube and 35  $\mu\text{m}$  per chamber. They are disposed orthogonally with respect to the beam axis, so they only provide a measurement of the  $\eta$  coordinate of the hits. The major limitation of the MDTs is that their drift time can reach up to 700 ns, limiting the maximum rate of operation of the system.

**Cathode Strip Chambers** The CSCs are multi-wire proportional chambers with a finer spatial resolution with respect to the MDTs. They are used in the first layer of the end-caps corresponding to  $2.0 < |\eta| < 2.7$ , where a higher rate of signal is expected due to the abundance of particles in the forward region.

**Resistive Plate Chambers** The RPCs are gas chambers mounted in the barrel system of the MS, in the pseudorapidity range  $|\eta| < 1.05$ . They are formed by two parallel plates, a positively-charged anode and a negatively-charged cathode, both made of a plastic material with high resistivity (Bakelite). The signal from ionising particles is collected by external metallic strips with a time resolution of the order of 1 ns, significantly shorter than the separation between two bunch crossings at the LHC (25 ns). They are used as inputs for the muon triggers, thanks to the fast speed of response, and they also measure the  $\phi$  coordinate of the muon hits, which is not provided by the MDTs.

**Thin Gap Chambers** The TGCs are multi-wire proportional chambers optimised to achieve a fast signal collection. They are mounted in the end-cap muon spectrometers to improve the muon trigger capability in the  $1.05 < |\eta| < 2.4$  region and to determine the  $\phi$  coordinate in the forward direction up to  $|\eta| = 2.7$ .

## 2.4 Trigger and data processing

In the ATLAS detector a complex Trigger system is thus present, interfaced with a Data Acquisition facility (DAQ, or TDAQ if the two systems are considered as a whole). A description of these fundamental components is given in the next two paragraphs, including a final brief overview of the Detector Control System (DCS).

### 2.4.1 Trigger system

As anticipated in Chapter 2, at design performance the rate of proton-proton collisions will reach approximately 40 MHz, corresponding to a theoretical average data flux of  $1.5 \text{ PBs}^{-1}$  if all the produced events were registered. Since such a huge amount of data is impossible to reconstruct and, in addition, the vast majority of proton collisions generate only irrelevant soft products, a trigger system dedicated to the recognition and selection of interesting events becomes an essential feature of the detector. Such a system must reduce the collected data to a rate below 400 Hz.

A scheme of the ATLAS trigger system is drawn in figure 2.13, showing the three prin-

cipal selection levels: Level-1 (L1) [76], Level-2 (L2) and Event Filter (EF). L2 and EF are often referred to as High Level Trigger (HLT) [77].

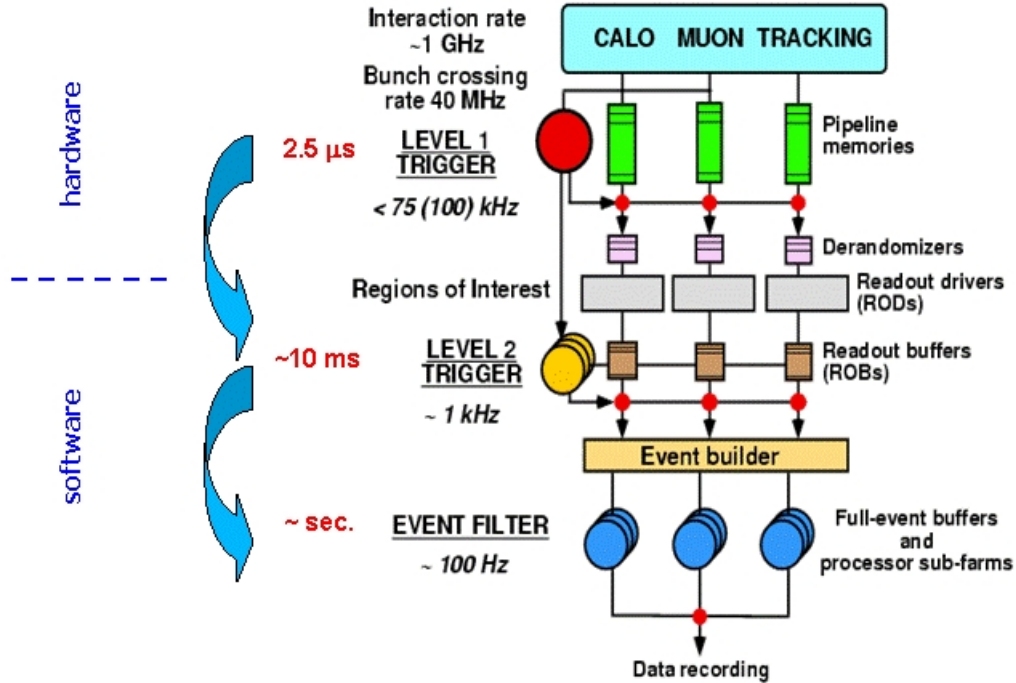


Figure 2.13: Scheme of the trigger chain of the ATLAS detector. The final collection rate has been increased to approximately 400 Hz.

The L1 trigger employs low granularity information from the calorimeter system and the Muon Spectrometer to perform a primary selection of events, putting them in correspondence with the correct bunch-crossing. The selection is based on the presence of relevant objects for the physics analyses, such as electrons, muons, photons, jets,  $\tau$  leptons or large missing transverse energy. A central trigger processor contains a large list of possible criteria for the selection and takes the decision in an average time of  $1 \mu\text{s}$ . Once an event is accepted, the information about the geometric ( $\eta, \phi$ ) coordinates of the identified objects is saved in the so called Regions-of-Interest (RoI), together with the type of selection that was passed. The output rate of L1 is about 100 kHz.

L2 combines the information from the RoIs (corresponding to the 1-2% of the total event size) with more inputs from the sub-detectors, performing an additional selection that reduces the event rate to an average of 3.5 kHz. Unlike L1, L2 employs software based algorithms, with an average processing time of 40 ms.

The last step of the trigger chain is the EF, that reconstructs the objects and takes the final decision on the events to be written to mass storage. The software is based on off-line al-

gorithms, optimized for the on-line time requirements. The output rate is approximately 400 Hz, and the single events are analyzed for about four seconds each.

### 2.4.2 Data acquisition and control system

The ATLAS trigger system is supported by a complex Data Acquisition (DAQ) system, that regulates the data flow from the output of the sub-detectors to the mass storage. Moreover, a Detector Control System is responsible for the overall detector performance. Each sub-detector produces a signal output that is first read by a L1-level front-end electronics, associated with specific Readout Drivers (RODs). The RODs meet general ATLAS requirements, in order to produce standard digital blocks that are readable by the Data Acquisition System. The front-end electronics is provided with an analogue-to-digital conversion system for the signal outputs of the sub-detectors, together with a buffer that is needed to retain the information for the time needed by the L1 trigger. The DAQ system receives its input from the front-end devices and stores the information about the RoIs in temporary buffers, in order to make it accessible to the L2 trigger. Finally, once the L2 trigger performs its selection, the system transfers the chosen set of events to the Event Filter and moves the resulting output to mass storage.

Finally, the Detector Control System is employed to monitor the hardware components of ATLAS, serving as a homogeneous interface that controls the general performance of the apparatus. By measuring and archiving many relevant operation parameters, the DCS is able to check if any deviation from the standard performances is present, and in these cases it also provides both manual and automatic corrections. Moreover, since it receives information from many detector components, it can coordinate the operation of the sub-detectors and the DAQ, and in addition it also regulates the interaction of the detector with external devices such as the LHC accelerator or the magnet system.

## 2.5 ATLAS physics program

To conclude this chapter, an overview of the ATLAS physics program is now given. It is important to recall that the same searches are targeted by the CMS collaboration, that exploits different detection technologies in order to reinforce the validity of the results.

### 2.5.1 Standard Model and Higgs measurements

Standard Model measurements in ATLAS are carried on for different purposes. First of all, well known processes such as the  $Z$  boson decay in two charged leptons are used

to calibrate the detector performances, thanks to the high level of precision that was reached by previous experiments. Indeed, the  $Z$  resonance has been measured for many years at LEP and its parameters are now known with great accuracy.

Although the LHC is essentially a discovery machine, large efforts are also dedicated to improve the precision of badly known Standard Model parameters. Together with representing an important research field on its own, this class of measurements is of particular interest for beyond Standard Model searches such as the one discussed in this thesis, since in this context Standard Model processes become relevant sources of background. For example, as will be discussed in the next chapters, the main background of the presented analysis comes from  $t\bar{t}$  pair production, therefore precise measurements from top quark studies are needed.

Finally, an extremely important class of measurements is the search for new Standard Model processes. Among these, the discovery of the Higgs boson discussed in the first chapter is certainly the most famous result, although other searches such as diboson production are also present. Now that the discovery is achieved, the Higgs group is struggling to provide as much information as possible about the new particle, in order to look for possible deviations from the behaviour predicted by the Standard Model. In general, any discrepancy between Standard Model predictions and observed data could be a great hint for new unknown physics.

### 2.5.2 Supersymmetry searches

This thesis is inserted in the framework of the ATLAS Supersymmetry searches, whose present results have already been discussed at the end of Chapter 1. The analyses performed with  $\sqrt{s} = 8$  TeV collisions have set several limits on SUSY particles, although many scenarios below the TeV scale are still possible. Relevant improvements in these searches are expected in Run 2, when a center of mass energy of 13 TeV will be reached. Since many solutions to open problems require the presence of light superpartners, if in Run 2 no evidence of SUSY particle is observed the theory will lose much of its interest.

### 2.5.3 Other searches

The ATLAS collaboration performs several exotic studies, probing many possible Standard Model extensions. An example are graviton searches, hinting at the discovery of quantum gravity scenarios, but efforts are dedicated also to leptoquarks, new gauge bosons and fourth generation particles. In addition, the possibility of an internal structure of quarks and leptons is also studied.

# **Chapter 3**

## **Object reconstruction**

# **Chapter 4**

## **B-tagging calibration with Monte Carlo simulations**

# **Chapter 5**

## **Search for bottom squark pair-production**

## **Chapter 6**

### **Search for top squark pair-production in RPV U1(B-L) scenarios**

# **Chapter 7**

## **Conclusions**

# **Appendix A**

## **Statistical tools**

# Bibliography

- [1] Michael E Peskin and Daniel V Schroeder. *An introduction to quantum field theory*; 1995 ed. Westview, Boulder, CO, 1995. Includes exercises.
- [2] S. L. Glashow. Partial Symmetries of Weak Interactions. *Nucl. Phys.*, 22:579–588, 1961.
- [3] Abdus Salam and John Clive Ward. Electromagnetic and weak interactions. *Phys. Lett.*, 13:168–171, 1964.
- [4] Steven Weinberg. A Model of Leptons. *Phys. Rev. Lett.*, 19:1264–1266, 1967.
- [5] H. Fritzsch, Murray Gell-Mann, and H. Leutwyler. Advantages of the Color Octet Gluon Picture. *Phys. Lett.*, 47B:365–368, 1973.
- [6] David J. Gross and Frank Wilczek. Ultraviolet Behavior of Nonabelian Gauge Theories. *Phys. Rev. Lett.*, 30:1343–1346, 1973.
- [7] F. Englert and R. Brout. Broken Symmetry and the Mass of Gauge Vector Mesons. *Phys. Rev. Lett.*, 13:321–323, 1964.
- [8] Peter W. Higgs. Broken Symmetries and the Masses of Gauge Bosons. *Phys. Rev. Lett.*, 13:508–509, 1964.
- [9] Peter W. Higgs. Broken symmetries, massless particles and gauge fields. *Phys. Lett.*, 12:132–133, 1964.
- [10] The ATLAS Collaboration. Observation of a new particle in the search for the Standard Model Higgs boson with the ATLAS detector at the LHC. *Phys. Lett.*, B716:1–29, 2012.
- [11] The CMS Collaboration. Observation of a new boson at a mass of 125 GeV with the CMS experiment at the LHC. *Phys.Lett.*, B716:30–61, 2012.

- [12] The ATLAS Collaboration. Measurement of the Higgs boson mass from the  $H \rightarrow \gamma\gamma$  and  $H \rightarrow ZZ^* \rightarrow 4\ell$  channels with the ATLAS detector using  $25 \text{ fb}^{-1}$  of  $pp$  collision data. *Phys. Rev.*, D90(5):052004, 2014.
- [13] The CMS Collaboration. Precise determination of the mass of the Higgs boson and tests of compatibility of its couplings with the standard model predictions using proton collisions at 7 and 8 TeV. *Eur. Phys. J.*, C75(5):212, 2015.
- [14] ATLAS and CMS Collaborations. Measurements of the Higgs boson production and decay rates and constraints on its couplings from a combined ATLAS and CMS analysis of the LHC pp collision data at  $\sqrt{s} = 7$  and 8 TeV. *JHEP*, 08:045, 2016.
- [15] Leonard Susskind. Dynamics of Spontaneous Symmetry Breaking in the Weinberg-Salam Theory. *Phys. Rev.*, D20:2619–2625, 1979.
- [16] Gerard 't Hooft. Naturalness, chiral symmetry, and spontaneous chiral symmetry breaking. *NATO Sci. Ser. B*, 59:135–157, 1980.
- [17] M. J. G. Veltman. The Infrared - Ultraviolet Connection. *Acta Phys. Polon.*, B12:437, 1981.
- [18] Gianfranco Bertone, Dan Hooper, and Joseph Silk. Particle dark matter: Evidence, candidates and constraints. *Phys. Rept.*, 405:279–390, 2005.
- [19] C. Giunti, C. W. Kim, and U. W. Lee. Running coupling constants and grand unification models. *Mod. Phys. Lett.*, A6:1745–1755, 1991.
- [20] Frank Wilczek David J. Gross, H. David Politzer. The 2004 Nobel Prize in Physics - Popular Information. *Nobel Media AB 2014*, 2004.
- [21] W. M. Alberico and S. M. Bilenky. Neutrino oscillations, masses and mixing. *Phys. Part. Nucl.*, 35:297–323, 2004. [Fiz. Elem. Chast. Atom. Yadra35,545(2004)].
- [22] Makoto Kobayashi and Toshihide Maskawa. CP Violation in the Renormalizable Theory of Weak Interaction. *Prog. Theor. Phys.*, 49:652–657, 1973.
- [23] M. B. Gavela, P. Hernandez, J. Orloff, and O. Pene. Standard model CP violation and baryon asymmetry. *Mod. Phys. Lett.*, A9:795–810, 1994.
- [24] J. Wess and B. Zumino. Supergauge Transformations in Four-Dimensions. *Nucl. Phys.*, B70:39–50, 1974.

- [25] Abdus Salam and J. A. Strathdee. Supersymmetry and Nonabelian Gauges. *Phys. Lett.*, 51B:353–355, 1974.
- [26] Sidney R. Coleman and J. Mandula. All Possible Symmetries of the S Matrix. *Phys. Rev.*, 159:1251–1256, 1967.
- [27] H. Weyl. Electron and Gravitation. 1. (In German). *Z. Phys.*, 56:330–352, 1929. [Surveys High Energ. Phys.5,261(1986)].
- [28] Glennys R. Farrar and Pierre Fayet. Phenomenology of the Production, Decay, and Detection of New Hadronic States Associated with Supersymmetry. *Phys. Lett.*, 76B:575–579, 1978.
- [29] Manuel Drees, Rohini Godbole, and Probir Roy. *Theory and phenomenology of Sparticles: an account of four-dimensional N=1 supersymmetry in high-energy physics*. World Scientific, Singapore, 2004.
- [30] K. Hidaka and A. Bartl. Impact of bosonic decays on the search for the lighter stop and sbottom squarks. *Phys. Lett.*, B501:78–85, 2001.
- [31] Stephen P. Martin. A Supersymmetry primer. *Adv.Ser.Direct.High Energy Phys.*, 21:1–153, 2010.
- [32] Riccardo Barbieri and G. F. Giudice. Upper Bounds on Supersymmetric Particle Masses. *Nucl. Phys.*, B306:63–76, 1988.
- [33] Michele Papucci, Joshua T. Ruderman, and Andreas Weiler. Natural SUSY Endures. *JHEP*, 09:035, 2012.
- [34] Zachary Marshall, Burt A. Ovrut, Austin Purves, and Sogee Spinner. Spontaneous  $R$ -Parity Breaking, Stop LSP Decays and the Neutrino Mass Hierarchy. *Phys. Lett.*, B732:325–329, 2014.
- [35] M. C. Gonzalez-Garcia, Michele Maltoni, Jordi Salvado, and Thomas Schwetz. Global fit to three neutrino mixing: critical look at present precision. *JHEP*, 12:123, 2012.
- [36] Christoph Borschensky, Michael Krämer, Anna Kulesza, Michelangelo Mangano, Sanjay Padhi, Tilman Plehn, and Xavier Portell. Squark and gluino production cross sections in pp collisions at  $\sqrt{s} = 13, 14, 33$  and  $100$  TeV. *Eur. Phys. J.*, C74(12):3174, 2014.

- [37] Daniele Alves et al. Simplified Models for LHC New Physics Searches. *J.Phys.*, G39:105005, 2012.
- [38] The ATLAS Collaboration. ATLAS Run 1 searches for direct pair production of third-generation squarks at the Large Hadron Collider. *Eur. Phys. J.*, C75(10):510, 2015. [Erratum: Eur. Phys. J.C76,no.3,153(2016)].
- [39] R. Gröber, Margarete M. Mühlleitner, E. Popenda, and A. Wlotzka. Light Stop Decays: Implications for LHC Searches. *Eur. Phys. J.*, C75:420, 2015.
- [40] Lyndon Evans and Philip Bryant. LHC Machine. *JINST*, 3:S08001, 2008.
- [41] The ATLAS Collaboration. The ATLAS Experiment at the CERN Large Hadron Collider. *JINST*, 3:S08003, 2008.
- [42] Oliver Sim Brüning, Paul Collier, P Lebrun, Stephen Myers, Ranko Ostojic, John Poole, and Paul Proudlock. *LHC Design Report v1*. CERN Yellow Reports: Monographs. CERN, Geneva, 2004.
- [43] John M. Campbell, J. W. Huston, and W. J. Stirling. Hard Interactions of Quarks and Gluons: A Primer for LHC Physics. *Rept. Prog. Phys.*, 70:89, 2007.
- [44] Ringaile Placakyte. Parton Distribution Functions. In *Proceedings, 31st International Conference on Physics in collisions (PIC 2011): Vancouver, Canada, August 28-September 1, 2011*, 2011.
- [45] Bora Isildak. *Measurement of the differential dijet production cross section in proton-proton collisions at  $\sqrt{s} = 7$  TeV*. PhD thesis, Bogazici U., 2011.
- [46] S. Myers and E. Picasso . The design, construction and commissioning of the CERN large Electron-Positron collider. *Contemporary Physics*, 31(6):387–403, 1990.
- [47] Design Report Tevatron 1 project. Technical Report FERMILAB-DESIGN-1984-01, 1984.
- [48] ALEPH, DELPHI, L3, OPAL, SLD Collaborations, LEP Electroweak Working Group, SLD Electroweak Group, and SLD Heavy Flavour Group. Precision electroweak measurements on the  $Z$  resonance. *Phys. Rept.*, 427:257–454, 2006.
- [49] The CDF Collaboration. Observation of top quark production in  $\bar{p}p$  collisions. *Phys. Rev. Lett.*, 74:2626–2631, 1995.

- [50] The D0 Collaboration. Observation of the top quark. *Phys. Rev. Lett.*, 74:2632–2637, 1995.
- [51] The ALEPH, DELPHI, L3, OPAL Collaboration, and the LEP Working Group for Higgs Boson Searches. Search for the standard model Higgs boson at LEP. *Phys. Lett.*, B565:61–75, 2003.
- [52] The CDF Collaboration. Combined search for the standard model Higgs boson decaying to a bb pair using the full CDF data set. *Phys. Rev. Lett.*, 109:111802, 2012.
- [53] The D0 Collaboration. Combined Search for the Standard Model Higgs Boson Decaying to  $b\bar{b}$  Using the D0 Run II Data Set. *Phys. Rev. Lett.*, 109:121802, 2012.
- [54] Michael Benedikt, Paul Collier, V Mertens, John Poole, and Karlheinz Schindl. *LHC Design Report v3*. CERN Yellow Reports: Monographs. CERN, Geneva, 2004.
- [55] ATLAS Luminosity Public Results. <https://twiki.cern.ch/twiki/bin/view/AtlasPublic/LuminosityPublicResults>.
- [56] The CMS Collaboration. The CMS Experiment at the CERN LHC. *JINST*, 3:S08004, 2008.
- [57] The LHCb Collaboration. The LHCb Detector at the LHC. *JINST*, 3:S08005, 2008.
- [58] The ALICE Collaboration. The ALICE experiment at the CERN LHC. *JINST*, 3:S08002, 2008.
- [59] The TOTEM Collaboration. The TOTEM experiment at the CERN Large Hadron Collider. *JINST*, 3:S08007, 2008.
- [60] The LHCf Collaboration. The LHCf detector at the CERN Large Hadron Collider. *JINST*, 3:S08006, 2008.
- [61] The MoEDAL Collaboration. Technical Design Report of the MoEDAL Experiment. Technical Report MoEDAL-TDR-001, 2009.
- [62] W. W. Armstrong et al. ATLAS: Technical proposal for a general-purpose p p experiment at the Large Hadron Collider at CERN. 1994.
- [63] The ATLAS Collaboration. ATLAS magnet system: Technical design report. *CERN-LHCC-97-18*, 1997.

- [64] G. Acquistapace et al. CMS, the magnet project: Technical design report. *CERN-LHCC-97-10*, 1997.
- [65] The ATLAS Collaboration. The ATLAS Inner Detector commissioning and calibration. *Eur. Phys. J.*, C70:787–821, 2010.
- [66] Norbert Wermes and G Hallewel. *ATLAS pixel detector: Technical Design Report*. Technical Design Report ATLAS. CERN, Geneva, 1998.
- [67] M Capeans, G Darbo, K Einsweiller, M Elsing, T Flick, M Garcia-Sciveres, C Gemme, H Pernegger, O Rohne, and R Vuillermet. ATLAS Insertable B-Layer Technical Design Report. Technical Report CERN-LHCC-2010-013. ATLAS-TDR-19, Sep 2010.
- [68] Malte Backhaus. The upgraded Pixel Detector of the ATLAS Experiment for Run2 at the Large Hadron Collider. Technical Report ATL-INDET-PROC-2015-015, CERN, Geneva, Dec 2015.
- [69] A. Abdesselam et al. The barrel modules of the ATLAS semiconductor tracker. *Nucl. Instrum. Meth.*, A568:642–671, 2006.
- [70] A. Abdesselam et al. The ATLAS semiconductor tracker end-cap module. *Nucl. Instrum. Meth.*, A575:353–389, 2007.
- [71] E. Abat et al. The ATLAS TRT barrel detector. *JINST*, 3:P02014, 2008.
- [72] E. Abat et al. The ATLAS TRT end-cap detectors. *JINST*, 3:P10003, 2008.
- [73] The ATLAS Collaboration. ATLAS liquid argon calorimeter: Technical design report. *CERN-LHCC-96-41*, 1996.
- [74] The ATLAS Collaboration. *ATLAS tile calorimeter: Technical Design Report*. Technical Design Report ATLAS. CERN, Geneva, 1996.
- [75] The ATLAS Collaboration. *ATLAS muon spectrometer: Technical Design Report*. Technical Design Report ATLAS. CERN, Geneva, 1997.
- [76] ATLAS first level trigger: Technical design report. 1998.
- [77] ATLAS high-level trigger, data acquisition and controls: Technical design report. 2003.